

Cosmic-ray antiproton constraints on light singlino-like dark matter candidates

David G. Cerdeño^{a,b}, Timur Delahaye^a, Julien Lavalley^{a,b,1}

^a*Instituto de Física Teórica (UAM/CSIC)*

Universidad Autónoma de Madrid, Cantoblanco, E-28049 Madrid — Spain

^b*Departamento de Física Teórica (UAM)*

Universidad Autónoma de Madrid, Cantoblanco, E-28049 Madrid — Spain

Abstract

The CoGeNT experiment, dedicated to direct detection of dark matter, has recently released excess events that could be interpreted as elastic collisions of ~ 10 GeV dark matter particles, which might simultaneously explain the still mysterious DAMA/LIBRA modulation signals, while in conflict with results from other experiments such as CDMS, XENON-100 and SIMPLE. It was shown that 5-15 GeV singlino-like dark matter candidates arising in singlet extensions of minimal supersymmetric scenarios can fit these data; annihilation then mostly proceeds into light singlet-dominated Higgs (pseudo)scalar fields. We develop an effective Lagrangian approach to confront these models with the existing data on cosmic-ray antiprotons, including the latest PAMELA data. Focusing on a parameter space consistent with the CoGeNT region, we show that the predicted antiproton flux is generically in tension with the data whenever the produced (pseudo)scalars can decay into quarks energetic enough to produce antiprotons, provided the annihilation S-wave is significant at freeze out in the early universe. In this regime, a bound on the singlino annihilation cross section is obtained, $\langle\sigma v\rangle \lesssim 10^{-26}$ cm³/s, assuming a dynamically constrained halo density profile with a local value of $\rho_{\odot} = 0.4$ GeV/cm³. Finally, we provide indications on how PAMELA or AMS-02 could further constrain or detect those configurations producing antiprotons which are not yet excluded.

Keywords:

dark matter; supersymmetry; singlet extended MSSM; direct detection; indirect detection; antimatter cosmic rays

Preprint: FTUAM-11-49, IFT-UAM/CSIC-11-41

1. Introduction

The CoGeNT [1] Collaboration has recently claimed for excess events in their data, while not confirmed by complementary searches like XENON-100 [2, 3] or SIMPLE [4]. Although CDMS-II had reported a few excess events [5], while not statistically significant, their latest results are also in conflict with the CoGeNT data [6]. The situation has become even more confusing, though quite exciting, since CoGeNT announced hints for annual modulation of the event counting rate [7]. Scatterings of weakly interacting massive particles (WIMPs) with masses around 10 GeV off the detector targets could explain these measurements, and interpretations in some specific particle physics models have been discussed in *e.g.* [8] and [9] (see also [10] for less conventional models). Intriguingly, this mass range turns out to be close to what is needed to fit the still mysterious DAMA/LIBRA signals [11, 12, 13]. Nevertheless, the authors of Ref. [9] have notably shown that some of the parameter space individually favored by the cited experiments may not be compatible among each other (see also [14, 15, 16]).

These controversial data have triggered a lot of activity in the field, and different phenomenological directions have been pursued. While light neutralinos arising from the minimal supersymmetric extension of the standard model (MSSM) are still debated (see arguments against this proposal in *e.g.* [17], to which very detailed highlights are opposed in [18]), singlet extensions of supersymmetric scenarios (including the next-to-MSSM — NMSSM) have received a particular attention, *e.g.* [19, 20, 21, 22, 23]. The NMSSM, which provides a very elegant way to solve the so-called μ -problem occurring in the MSSM (see [24, 25] for reviews), could actually lead to a phenomenology consistent with the direct detection hints, though not generically, and some interesting regions of the parameter space are worth being investigated more deeply [26, 21, 22]. In slight contrast, more general singlet extensions uncorrelated with the μ -problem can quite easily be tuned to accommodate the data, *e.g.* [23], because more flexible. In these models, the dark matter candidate is usually a light singlino-dominated neutralino.

Interesting constraints on light WIMPs may actually come from colliders [27, 28, 29], but most of the singlet models mentioned above seem to escape them [21, 22]. From the astrophysical point of view, the annihilation of such light WIMPs may also generate gamma-ray fluxes at the edge of being excluded with current measurements [30]; observational limits on high-energy neutrinos from the Sun also give interesting constraints,

Email addresses: davidg.cerdeno@uam.es (David G. Cerdeño), timur.delahaye@uam.es (Timur Delahaye), lavalley@in2p3.fr (Julien Lavalley)

¹Multidark fellow

as shown in *e.g.* [31]. Another very powerful astrophysical constraint comes from measurements of local cosmic-ray antiprotons, which severely limits *direct* annihilation into quarks [32]. In this paper, we aim at extending the latter analysis to singlet-like phenomenologies in which singlino-like dark matter particles χ annihilate into light scalar and/or pseudo-scalar particles (generically referred to h and a in the following), which can further decay, for instance into quarks. For the sake of generality, we will adopt a model-independent approach by using an effective Lagrangian relevant to any particular singlet model, and will derive constraints on all involved masses and couplings. We note that indirect detection constraints come into play only when annihilation is not velocity-suppressed, which implies that the dominant annihilation channel is $\chi\chi \rightarrow ah$. This defines the mass range we are going to focus on, namely $2m_\chi \geq m_a + m_h$.

The outline of the paper is the following. In Sect. 2, we present our effective Lagrangian approach and discuss the annihilation cross section and issues related to the relic density. In Sect. 3, we briefly review the calculation of the spin-independent WIMP-nucleus cross section, and delineate the parameter space to be considered for interpretations of the direct detection hints. In Sect. 4, we derive the cosmic-ray antiproton spectra generated by decays of light scalar and pseudo-scalar Higgs bosons, and we determine the constraints current flux measurements put on the effective parameter space. We conclude in Sect. 5. Further details on our calculations are given in the appendices.

2. Effective Lagrangian approach to singlino-like dark matter scenarios

The phenomenology of light singlino-like dark matter scenarios is mostly set by (i) the couplings between the neutralino, a Majorana fermion, and the light scalar and pseudo-scalar particles of the Higgs sector, (ii) the masses of the involved fields, and (iii) the couplings of the light scalars to standard model particles. We address the former point here; the latter will be discussed in Sect. 2.2. Denoting χ the neutralino field and ϕ_i a generic field that contains a scalar part h_i and a pseudo-scalar part a_i such that $\phi_i \equiv h_i + i a_i$, we consider the following effective interaction Lagrangian:

$$\mathcal{L}_{\text{eff}} = -\frac{1}{2} \sum_i \bar{\chi} C_{\chi i} \chi \phi_i - \sum_{i,j,k} \frac{\lambda_{ijk}}{\eta_{ijk}} \phi_i \phi_j \phi_k + \text{h.c.}, \quad (1)$$

where we $\lambda_{i,j,k}$ is a dimensional real coupling (η_{ijk} is a combinatorial factor), and where

$$C_{\chi i} \equiv c_{\chi i} + i \tilde{c}_{\chi i} \gamma_5 = \bar{C}_{\chi i} \quad (2)$$

features both the couplings of the scalar and pseudo-scalar fields ϕ_i to the dark matter fermionic field χ . We further define $c_{\chi i}$ (scalar coupling) and $\tilde{c}_{\chi i}$ (pseudo-scalar coupling) as real numbers.

2.1. Higgs sector

We consider singlet extensions of the MSSM in which the lightest neutralino is singlino dominated, and the light Higgs scalar and pseudo-scalar are singlet dominated. Nevertheless, the physical Higgs fields are still mixtures of the Higgs doublets H_u and H_d and of the singlet field S , which allows us to define the mixing matrix \mathcal{S} as

$$\mathcal{S}_i^j = \begin{pmatrix} s_\theta s_\varphi & -c_\theta s_\varphi & c_\varphi \\ -c_\theta s_\varphi - s_\theta c_\psi c_\varphi & c_\theta c_\psi c_\varphi - s_\theta s_\psi & c_\psi s_\varphi \\ c_\theta c_\psi - s_\theta s_\psi c_\varphi & c_\theta s_\psi c_\varphi - c_\theta c_\psi & s_\psi s_\varphi \end{pmatrix}, \quad (3)$$

where s_k and c_k stand for $\sin k$ and $\cos k$, respectively. The mass eigenstates corresponding to the lightest pseudo-scalar and scalar fields, which we respectively denote a and h , are conventionally given by the first row:

$$\begin{aligned} h &= s_\varphi [s_\theta \text{Re}(H_d) - c_\theta \text{Re}(H_u)] + c_\varphi \text{Re}(S) \\ a &= s_{\varphi_a} [s_{\theta_a} \text{Im}(H_d) - c_{\theta_a} \text{Im}(H_u)] + c_{\varphi_a} \text{Im}(S) \\ &= s_{\varphi_a} [A_{\text{MSSM}}] + c_{\varphi_a} \text{Im}(S), \end{aligned} \quad (4)$$

where A_{MSSM} corresponds to the same linear combination of the imaginary parts of H_u and H_d that describes the pseudo-scalar Higgs in the MSSM. The mixing angles can be determined in specific models from the mass terms and couplings featuring the superpotential and the soft potential. The Higgs mixing will actually play an important role not only when calculating the direct detection signals, as discussed in Sect. 3, but also to determine the decay channels of the light Higgs fields, which the antiproton production depends on (see Sect. 4.1). It also helps us understanding the collider constraints, as discussed later on.

In this paper, we are assuming the lightest CP-even Higgs to be singlet-like, in order to avoid collider constraints, and therefore we take $c_\varphi \geq 0.9$. For the two heavy CP-even Higgs bosons, we adopt a MSSM-like scenario in which the lightest one is of u -type (H_u) and the heavy one is approximately H_d . Thus, we fix $c_\theta = c_\psi = 0.9$.

Last but not least, as it is customary in the MSSM, we define $\tan\beta$ as the ratio of the Higgs doublet fields vacuum expectation values, $\tan\beta \equiv \langle H_u \rangle / \langle H_d \rangle$.

2.2. Couplings to standard model fermions

To complement this effective setup, we also need to define the couplings between the scalar and pseudo-scalar fields to the standard model (SM) fermions, which will further determine the branching ratios of their decay products (annihilation final states) and the strength of the WIMP-nucleon interaction (direct detection signals). For a field ϕ_i having both a scalar and a pseudo-scalar part, the couplings to SM fermion fields differs for up-type quarks (or neutrinos) and down-type quarks (or charged leptons) as:

$$\begin{aligned} C_{\phi_i, \text{up,up}} &= -\frac{g m_u}{2 M_W s_\beta} \left\{ s_\varphi c_\theta - i \gamma_5 s_{\varphi_a} c_{\theta_a} \right\} \\ C_{\phi_i, \text{down,down}} &= -\frac{g m_d}{2 M_W c_\beta} \left\{ s_\varphi s_\theta - i \gamma_5 s_{\varphi_a} s_{\theta_a} \right\}, \end{aligned} \quad (5)$$

where m_u (m_d) is the up-type (down-type) quark mass.

These couplings are useful to compute the decay branching ratios of the light Higgs fields, which will further determine the induced antiproton spectrum. In practice, we use the light (pseudo-)scalar decay widths that we derive as:

$$\begin{aligned}\Gamma_{\phi_i \rightarrow f\bar{f}} &= N_c \frac{C_{\phi_i, f, \bar{f}}^2}{8\pi} m_{\phi_i} \left[1 - \left(\frac{2m_f}{m_{\phi_i}} \right)^2 \right]^{3/2} \\ \Gamma_{\phi_i \rightarrow \phi_j^* \phi_j^*} &= \frac{\lambda_{ijk}^2}{32\pi m_{\phi_i}} \sqrt{1 - \left(\frac{2m_{\phi_j}}{m_{\phi_i}} \right)^2},\end{aligned}\quad (6)$$

where N_c is a color factor (3 for quarks, 1 for leptons), and the latter expression is relevant to the cases where the process $h \rightarrow a a$ adds up to decays into SM fermions ($m_h \geq 2m_a$).

In the following, we will only consider those interactions between singlinos and SM particles which are mediated by the scalar and pseudo-scalar Higgs bosons, assuming all other contributions to be negligible. In other words, we assume that other sectors of the complete underlying theory decouple. This is a reasonable assumption given the current mass limits on squarks [33, 34] and charged sleptons [35]. Moreover, as regards the Higgs sector, we impose that the interactions with standard matter are driven by light field exchanges only (see Sect. 3).

2.3. Some collider constraints

It is important to derive ranges for our effective model parameters, namely masses, mixing angles and couplings, which are consistent with current collider constraints. These constraints necessarily involve the couplings to SM particles, which have been made explicit in Eq. (5). We basically use the constraints provided in [23] for light scalars, and in [36] for light pseudo-scalars. The only additional feature we impose to our singlino dark matter candidate is to reproduce the region compatible with the WIMP interpretation of the CoGeNT signal, given the parameter space delineated for the scalar and pseudo-scalar fields below.

Limits can be derived because of the potential contributions light scalars and pseudo-scalars may give to rare mesons decays. From measurements of B decays by Belle [37] and SM background calculations by [38], the following limit has been derived by the authors of [23] for the light scalar mass, given its non-singlet content s_φ :

$$\begin{aligned}\text{Br}(B \rightarrow h + X_s) \times \text{Br}(h \rightarrow \mu^+ + \mu^-) &= \\ 0.058 \left[\frac{s_\varphi}{0.1} \right]^2 \left[1 - \frac{m_h^2}{m_b^2} \right]^2 \times \text{Br}(h \rightarrow \mu^+ + \mu^-) &< 2.5 \times 10^{-6}.\end{aligned}\quad (7)$$

The decay branching ratio $\text{Br}(h \rightarrow \mu^+ + \mu^-)$ is readily computed from Eq. (5). This roughly sets a lower limit for m_h in terms of the bottom quark mass, namely $m_h \gtrsim m_b$.

There is an additional and independent limit on s_φ which can be derived from LEP data on Higgs searches, especially from the process $e^+ e^- \rightarrow Zh \rightarrow \nu \bar{\nu} h$ [39]. This yields the upper limit $s_\varphi \lesssim 0.08$, valid as long as $m_h < 2m_a$, *i.e.* as long as the decay channel $h \rightarrow a a$ is forbidden [23].

Constraints on the singlet content of the pseudo-scalar can be extracted from *e.g.* the CLEO Higgs search data from the $\Upsilon(1S)$ decays [40]. They are expressed in terms of the reduced coupling X_d of the light pseudo-scalar a to down-type quarks and leptons, which is normalized with respect to the coupling of the CP-even SM Higgs boson, and a very conservative limit is given by:

$$X_d = s_{\varphi_a} \tan \beta < 0.5, \quad (8)$$

as read off from Fig. 1 of Ref. [36]. This is definitely not a stringent limit for the phenomenology under scrutiny here, since this has no consequence on the pseudo-scalar decay products (the mixing angles factorize out in the decay branching ratios). This still ensures that the singlino annihilation into SM fermions via light pseudo-scalar exchange is always suppressed with respect to the annihilation into light (pseudo-)scalars.

Finally, we set a lower limit of $m_a \geq 1$ GeV in the following to avoid relying on too large fine-tuning zones in more theoretically constrained parameter spaces.

2.4. Relic density

One of the most important constraints on dark matter models obviously comes from requiring that they lead to the correct cosmological abundance, which usually severely reduces the available parameter space. Despite the uncertainties affecting our knowledge of the expansion rate of the universe before the big-bang nucleosynthesis (BBN) (see *e.g.* [41]), the general formalism to derive the relic abundance, based on solving a covariant Boltzmann equation, has been established and tested for a long time [42, 43, 44, 45, 46, 47]. There are some public codes like DarkSUSY [48] or MicrOMEGAs [49], which numerically solve the Boltzmann equation, originally designed for supersymmetric models. Both these codes essentially make use of the same numerical scheme and of the same tables for the effective degrees of freedom, which rely on earlier works [44, 46, 47]. Consequently, differences between them are expected to come from the annihilation cross section calculation only. An alternative to these numerical tools, but at the cost of loose accuracy, is to use approximate analytical expressions [45, 46, 50]. Here, we use our own numerical tools, more detailed in Appendix B to which we refer the reader for the definitions of the relevant parameters. Denoting $Y_{>f}$ the comoving dark matter density after decoupling such that $Y_{>f} \gg Y_{\text{eq}}$, its value today Y_0 can be calculated from the following expression:

$$Y_0 = \left\{ \frac{1}{Y_{>f}} + \sqrt{\frac{\pi}{45}} m_\chi M_p \int_{x_{>f}} dx \frac{g_\star^{1/2} \langle \sigma v \rangle}{x^2} \right\}^{-1}, \quad (9)$$

where $x = m_\chi/T$ (T is the thermal plasma temperature). Note that the second term in the right-hand side, featuring the annihilation cross section $\langle \sigma v \rangle$ (see Sect. 2.5) and the effective degrees of freedom g_\star , is usually dominant. A numerical code is basically useful to compute $Y_{>f} = Y(x_{>f})$ to a good accuracy from the full Boltzmann equation (see Eq. B.1 in Appendix B), given the temperature-dependent annihilation cross section

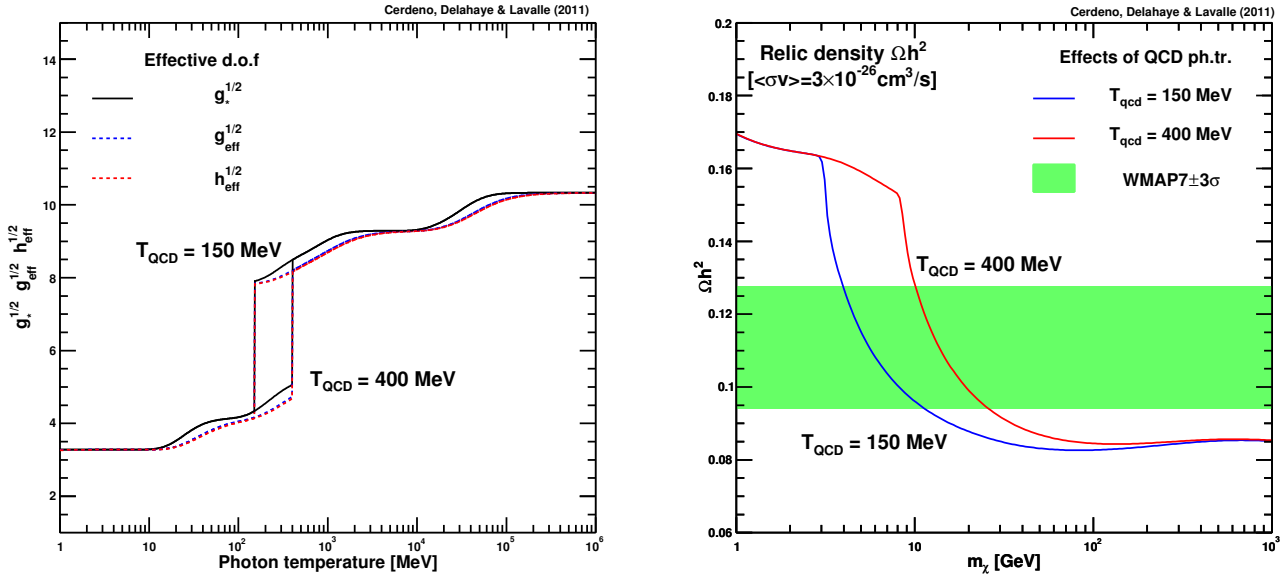


Figure 1: Left: effective degrees of freedom relevant to the relic density calculation, where a sharp first order QCD phase transition is assumed. Right: impact of assuming different QCD phase transition temperature on the relic abundance of Majorana fermions — we fix the annihilation cross-section to $3 \times 10^{-26} \text{ cm}^3/\text{s}$ for the sake of illustration.

$\langle\sigma v\rangle$ and the effective degrees of freedom g_* . The relic abundance then merely reads:

$$\begin{aligned} \Omega_\chi h^2 &= m_\chi \frac{s_0 Y_0 h^2}{\rho_c} = m_\chi \frac{8\pi M_p^2 s_0 Y_0}{3 \times 100^2} \\ &\simeq 2.744 \times 10^8 m_\chi Y_0, \end{aligned} \quad (10)$$

where we have translated the critical density ρ_c in terms of the Hubble parameter H , using the relation $H^2 = (100 \times h)^2 = 8\pi\rho_c/3$. The parameter $s_0 \simeq 2891.23 \text{ cm}^{-3}$ is the entropy density today — we have taken a CMB temperature of 2.72548° K [51].

One of the key issues in calculating the relic density of $\sim 10 \text{ GeV}$ WIMPs is the QCD phase transition. Indeed, these WIMPs typically decouple at temperatures $T_f \sim m_\chi/20 \sim 400 \text{ MeV}$, when quarks (and gluons) go from asymptotic freedom to confinement into hadrons. This transition is therefore characterized by an important change in the relativistic degrees of freedom g_* appearing in Eq. (9), which can be a source of systematic errors in the predictions (as was already clear from *e.g.* Figs. 5 and 6 of [44]). For instance, slightly modifying the phase transition temperature T_{QCD} can lead to significant changes in the final relic abundance, by up to 50% (a factor of ~ 4 in g_*), for those models which happen to decouple after instead of before the transition, after modification of T_{QCD} (see Eq. 9). The point is that we do not know much about this phase transition yet despite the recent progresses obtained in lattice QCD [52], and theoretical uncertainties in this regime might still be sizable [53]. The current state of the art [54] is implemented in *e.g.* DarkSUSY, but modifications of the transition temperature is not user-free.

To try to bracket potential theoretical uncertainties coming from this phase transition, we have recomputed the effective

degrees of freedom g_* for different values of T_{QCD} , considering a close to first order phase transition. An example is shown in the left panel Fig. 1, where we display $g_{\text{eff}}^{1/2}$, $h_{\text{eff}}^{1/2}$ and $g_*^{1/2}$ for two different assumptions $T_{\text{QCD}} = 150$ or 400 MeV (see Eq. B.2 in Appendix B for the definitions). The right panel exhibits the consequence on the dark matter relic abundance, assuming a constant annihilation cross section set to its canonical value $\langle\sigma v\rangle = 3 \times 10^{-26} \text{ cm}^3 \text{ s}^{-1}$, and only varying the WIMP mass m_χ . We clearly see that in the region of interest, $m_\chi \sim 10 \text{ GeV}$, the relic density can decrease or increase by a factor of ~ 2 , depending on whether decoupling occurs just before or just after the QCD phase transition — this can be understood from Eq. (9), where we see that $Y_0 \propto (g_*^{1/2} \langle\sigma v\rangle)^{-1}$. Therefore, some models in this mass range can easily be cosmologically excluded for one choice of T_{QCD} but allowed for other choices. In the plot, as will be the case in the rest of the paper, we have used the WMAP-7 data for the present dark matter abundance, *i.e.* $\Omega_\chi h^2 = 0.1109 \pm 0.0056$ [55], which appears as the green band.

This illustrates why uncertainties on the quark-hadron transition and on T_{QCD} should be taken into account, as often underlined in the past, like in [56]. A detailed implementation of this transition is beyond the scope of this paper. Still, we consider the two extreme cases depicted in the left panel of Fig. 1, which is likely sufficient to encompass the full theoretical error. Finally, we stress that the impact on indirect detection signals amounts to the same factor of ~ 2 . The annihilation cross section needs to be relatively larger to get the correct abundance when dark matter particles decouple after the QCD phase transition, as clearly seen in the right panel of Fig. 1. We have checked that using other predictions for the evolution of the relativistic degrees of freedom and their change during the QCD

phase transition, for instance those included in the DarkSUSY package, led to a $\lesssim 10\%$ difference in the relic density predictions, or equivalently in the annihilation cross section². Therefore, taking a 3- σ band for $\Omega_\chi h^2$ is well enough to encompass the theoretical uncertainties in the effective degrees of freedom for a given T_{QCD} . Thus, we will consider any configuration as cosmologically relevant whenever leading to a relic density of $\Omega_\chi h^2 = 0.1109 \pm 0.0168$.

2.5. Annihilation cross section

The annihilation cross section is relevant not only to indirect detection, but also to direct detection, since in both cases it determines the cosmological abundance today. In the following, we assume that the only particles involved in the annihilation process are the light scalar and pseudo-scalar Higgs bosons, h and a respectively. This is justified by the fact that we are in the very light mass and singlet/singlino dominated regime — other Higgs bosons, charginos and sfermions have much larger masses, while similar couplings. In such a regime, annihilation implies the following final states: $\chi\chi \rightarrow aa$, $\chi\chi \rightarrow hh$ and $\chi\chi \rightarrow ah$, which can be summarized thanks to the Feynman diagrams represented in Fig. 2.

As it is well known (e.g. [57]), $\chi\chi \rightarrow ah$ is the only tree-level process among the three above possibilities to have a non-vanishing zero-velocity limit, i.e. the only process relevant to indirect detection. It is kinematically allowed as long as $2m_\chi \geq m_a + m_h$, which defines the mass range we are dealing with in this analysis. The full calculation of the annihilation cross section is detailed in Appendix A. Here, we just summarize a few helpful results. It usually proves interesting to expand the thermally averaged annihilation cross section as a power series of the inverse of the variable $x \equiv m_\chi/T \propto v^{-2}$ ($x_f \sim 20$ at freeze out, and $x_0 \sim 10^7$ in the Galaxy today):

$$\langle\sigma v\rangle = a + b/x + \mathcal{O}(x^{-2}). \quad (11)$$

Both coefficients a and b take analytical expressions in the present study. The S-wave contribution is given by (we neglect the widths of the exchanged particles³):

$$a = a_{\chi\chi \rightarrow ah} = \frac{\sqrt{\left(1 - \left[\frac{(m_a+m_h)}{2m_\chi}\right]^2\right)\left(1 - \left[\frac{(m_a-m_h)}{2m_\chi}\right]^2\right)}}{16\pi m_\chi^2} \times \quad (12)$$

$$\frac{\tilde{c}_{\chi\chi a}^2}{\left(4m_\chi^2 - m_a^2\right)^2 \left(1 - \frac{(m_a^2+m_h^2)}{4m_\chi^2}\right)^2} \times$$

$$\left[c_{\chi\chi h} \left(4m_\chi^2 - m_a^2\right) \left(1 + \frac{(m_a^2 - m_h^2)}{4m_\chi^2}\right) - \right.$$

$$\left. \lambda_{aah} m_\chi \left(1 - \frac{(m_h^2 + m_a^2)}{4m_\chi^2}\right) \right]^2.$$

²We have also made some comparisons between our calculation and the one provided in MicrOMEGAS, and found an agreement within $\sim 1\%$ when using the MicrOMEGAS table for the degrees of freedom (identical to the DarkSUSY table).

³Particle widths are included in the full numerical calculation.

This equation fully sets the annihilation cross section for the indirect detection signals that we will consider later. We immediately see that there is a competition between the s and t/u diagrams through the couplings λ_{aah} and $c_{\chi\chi h}$. Note that the latter is also the one that fixes the contributions of CP-even Higgs bosons to the direct detection signal (more details in Sect. 3), which sketches a way to link the indirect detection constraints to the direct detection signal: the relation is straightforward in the case $\lambda_{aah} = 0$, corresponding not only to the suppression of the s -channel of $\chi\chi \rightarrow ah$ but also of that of process $\chi\chi \rightarrow aa$. Finally, for $\lambda_{aah} \sim c_{\chi\chi h}$ and close-to-degenerate masses, the t/u diagram dominates the cross section, which again induces a significant correlation between the direct detection signal and the indirect detection constraints.

We also remark that the coupling $c_{\chi\chi a}$ does drive the a -term amplitude, which is actually quite obvious since $\chi\chi$ is bound to be a pseudo-scalar state at null velocity. Suppressing this coupling is a very simple way to avoid indirect detection constraints. In that case, annihilation before freeze-out would proceed mostly through $\chi\chi \rightarrow hh$, but also partly through $\chi\chi \rightarrow aa$ via the s -channel, provided these final states are kinematically allowed.

Although the connection between the elastic interaction with nuclei and the annihilation into ah may be understood from the above equation, we still have to make sure that the a -term of the cross section expansion is the dominant one in the early universe, in order for it to be fixed by the relic abundance. Indeed, should the processes $\chi\chi \rightarrow aa, hh$ be dominant at freeze out, then that would lessen the bounding strength of indirect detection and also make us lose potential correlations between direct and indirect signals. We recall that the correlation is definitely lost when $m_\chi \geq m_h$ (m_a) and $2m_\chi < m_a + m_h$, for which $\chi\chi \rightarrow hh$ (aa) is the only annihilation possibility left; we do not consider such cases here.

For completeness, we provide the first order terms b_{aa} and b_{hh} associated with annihilation into aa and hh , which drive the relic density when $2m_\chi < m_a + m_h$ (still neglecting the particle widths):

$$b_{aa} = \frac{\sqrt{1 - m_a^2/m_\chi^2}}{64\pi (2m_\chi^2 - m_a^2)^4} \times \quad (13)$$

$$\left[16\tilde{c}_{\chi\chi a}^4 m_\chi^2 (m_\chi^2 - m_a^2)^2 + \right.$$

$$8\lambda_{aah} c_{\chi\chi h} \tilde{c}_{\chi\chi a}^2 m_\chi (2m_\chi^2 - m_a^2)^2 \frac{(m_\chi^2 - m_a^2)}{(4m_\chi^2 - m_h^2)}$$

$$\left. + 3(\lambda_{aah} c_{\chi\chi h})^2 \frac{(2m_\chi^2 - m_a^2)^4}{(4m_\chi^2 - m_h^2)^2} \right];$$

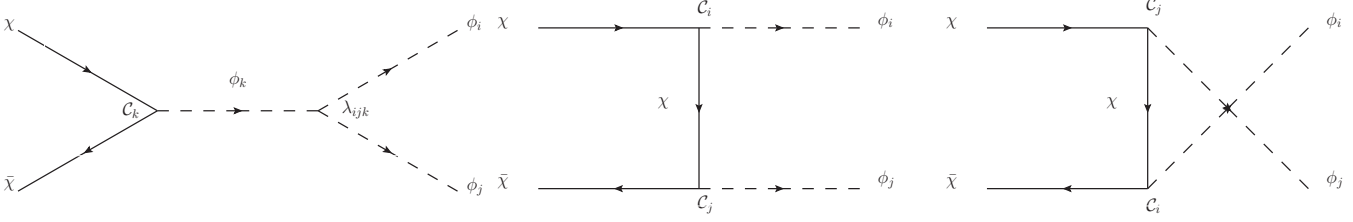


Figure 2: Feynman diagrams relevant to the $\chi\chi$ annih

$$b_{hh} = \frac{c_{\chi\chi h}^2 \sqrt{1 - m_h^2/m_\chi^2}}{64\pi (2m_\chi^2 - m_h^2)^4} \times \quad (14)$$

$$\left[16 c_{\chi\chi h}^2 m_\chi^2 (9m_\chi^4 + 2m_h^4 - 8m_h^2 m_\chi^2) - \right.$$

$$8m_\chi \lambda_{hhh} c_{\chi\chi h} (2m_\chi^2 - m_h^2)^2 \frac{(5m_\chi^2 - 2m_h^2)}{(4m_\chi^2 - m_h^2)} +$$

$$\left. 3\lambda_{hhh}^2 \frac{(2m_\chi^2 - m_h^2)^4}{(4m_\chi^2 - m_h^2)^2} \right].$$

These terms are the leading terms of the annihilation cross section when $2m_\chi < m_a + m_h$. We emphasize that even in the case $2m_\chi \geq m_a + m_h$, *i.e.* when a_{ah} is not suppressed, the velocity-dependent terms can not only partly contribute to the full annihilation cross section at decoupling in the early universe (up to ~ 10 - 20% when couplings and masses are taken similar, and considering also b_{ah} , not given here), but can also dominate in some cases, *e.g.* when the coupling $\tilde{c}_{\chi\chi a}$ is suppressed. This means that the full annihilation cross section needs to be considered for relic density calculations, which we have done in this study. In fact, we did not use this Taylor expansion approach to compute the thermal average of σv in the relic density calculation, but the exact numerical method presented in [46, 47]. Still, the velocity independent term a_{ah} given in Eq. (12) fully characterizes the annihilation cross section relevant to indirect detection. Moreover, Eqs. (13) and (14) will prove very useful to interpret the antiproton constraints (see Sect. 4).

3. Direct detection of singlino-like particles

In this paper, we aim at confronting the light singlino parameter space compatible with the CoGeNT region to the antiproton constraints. It is therefore important to provide some details on how the CoGeNT region can be covered in the frame of our effective approach.

The singlino couplings to the Higgs mass eigenstates will be denoted as $c_{\chi j}$, in consistency with the Lagrangian introduced in Eq. (1).

Elastic collision of a singlino off a target nucleus would take place through the exchange of a CP-even Higgs along a t -channel, as depicted in Fig. 3. This scattering can be described in terms of an effective Lagrangian [57],

$$\mathcal{L}_{eff} \supset \alpha_{q_i} \bar{\chi} \chi \bar{q}_i q_i, \quad (15)$$

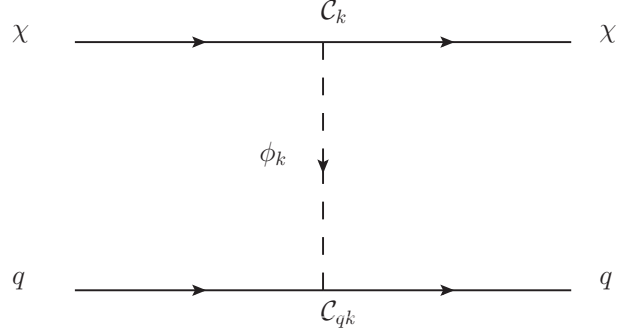


Figure 3: Diagram describing the elastic interaction of a singlino with a quark.

where the coupling α_{q_i} results from adding the contributions of the exchanges of the three CP-even Higgs bosons and reads,

$$\alpha_{q_i} \equiv \sum_{j=1}^3 \frac{g m_{q_i}}{2M_W B_i} \frac{c_{\chi j}}{m_{H_j}^2} \mathcal{S}_j^{3-i}, \quad (16)$$

where $i = 1, 2$ for up(down)-type quarks, $B_1 = \sin\beta$ and $B_2 = \cos\beta$. The mixing matrix \mathcal{S} has been defined in Eq. (3). Note that the term of the above sum corresponding to our light Higgs boson h can be straightforwardly rewritten as $\alpha_{q_i}^h = c_{\chi j} C_{hq\bar{q}}/m_h^2$, where the coupling $C_{hq\bar{q}}$ has been defined in Eq. (5).

The total spin-independent WIMP-proton scattering cross section yields

$$\sigma_{\chi-p}^{SI} = \frac{4}{\pi} \frac{m_p^2 m_\chi^2}{(m_p + m_\chi)^2} f_p^2, \quad (17)$$

where m_p is the proton mass and

$$\frac{f_p}{m_p} = \sum_{q_i=u,d,s} f_{Tq_i}^p \frac{\alpha_{q_i}}{m_{q_i}} + \frac{2}{27} f_{TG}^p \sum_{q_i=c,b,t} \frac{\alpha_{q_i}}{m_{q_i}}. \quad (18)$$

The quantities $f_{Tq_i}^p$ and f_{TG}^p are the hadronic matrix elements which parameterize the quark content of the proton (the second term is due to the interaction of the WIMP with the gluon scalar density in the nucleon). We will use $f_u^p = 0.023$, $f_d^p = 0.033$ and $f_s^p = 0.26$ which follows from the latest results on the pion-nucleon sigma-term [58], which affects the determination of the strange content of the quark.

The leading term in the scattering cross section is usually due to the coupling to the s quark (the contribution from quarks u and d being almost negligible and that from f_{TG}^p being at least a factor 5 smaller in the determination of f^p). Under this assumption it is possible to derive from Eq. (16) a condition for

the lightest Higgs contribution to be the dominant one in terms of the Higgs masses and the various couplings. In particular, we will demand

$$\left| \frac{c_{\chi 1}}{m_{H_1^0}^2} \mathcal{S}_1^1 \right| > 10 \left| \frac{c_{\chi 2}}{m_{H_2^0}^2} \mathcal{S}_2^1 \right|, \quad (19)$$

and

$$\left| \frac{c_{\chi 1}}{m_{H_1^0}^2} \mathcal{S}_1^1 \right| > 10 \left| \frac{c_{\chi 3}}{m_{H_3^0}^2} \mathcal{S}_3^1 \right|. \quad (20)$$

Notice that since we are considering very small masses for the lightest Higgs boson, these conditions are normally easy to fulfil. In our case they will imply a constraint on the Higgs doublet contribution and on the neutralino-Higgs coupling. For example, for a typical configuration with $m_{H_1^0} = 10$ GeV and $m_{H_2^0} = 120$ GeV the above condition implies $c_{\chi 1} \mathcal{S}_1^1 > 7 \times 10^{-2} c_{\chi 2} \mathcal{S}_2^1$. Under these conditions the spin-independent cross-section can be approximately expressed as

$$\sigma_{\chi-p}^{\text{SI}} \approx \frac{m_p^4 m_\chi^2}{\pi(m_p + m_\chi)^2} \left(\frac{g f_s^p}{M_W} \right)^2 \left(\frac{c_{\chi 1} \mathcal{S}_1^1}{m_{H_1^0}^2 c_\beta} \right)^2 \quad (21)$$

In order to explore the region consistent with the latest hints for very light WIMPs in direct detection experiments [12, 1, 7], we have constrained the input parameters to produce a singlino-proton spin-independent cross section between 3×10^{-5} pb and 3×10^{-4} pb, and singlino masses in the range 6 – 15 GeV. This window in the $(\sigma_{\chi-p}^{\text{SI}}, m_\chi)$ plane contains the region compatible with the first observation by the CoGeNT collaboration [1] and is extended in order to account for variations of this region when astrophysical uncertainties are taken into account [9, 59] and to include the area consistent with DAMA/LIBRA result if interpreted in terms of WIMP recoils on NaI (assuming negligible channeling). Of course, the region consistent with the latest data release by CoGeNT [7] is also contained in the whole area.

To try to delineate a parameter space as complete as possible, we have performed different random scans over the full parameter space defined by the involved free masses and couplings, taking different values of $\tan\beta$ for each. Since we require a given range of spin-independent cross-section and, as we said above, we consider only those cases where the lightest Higgs contribution to $\sigma_{\chi-p}^{\text{SI}}$ is dominant, this implies a constraint on the lightest Higgs composition and its coupling to singlinos. In particular, for $m_\chi = 6 - 15$ GeV, Eq. (21) leads to

$$3 \times 10^{-4} \text{ GeV}^{-2} \lesssim \left| \frac{c_{\chi 1} \mathcal{S}_1^1}{m_{H_1^0}^2 \cos\beta} \right| \lesssim 9 \times 10^{-4} \text{ GeV}^{-2}. \quad (22)$$

We note that this condition implies that for large values of $\tan\beta$ the necessary value of the coupling $c_{\chi 1}$ in order to reproduce the CoGeNT data can be smaller.

In practice, the various input parameters have been randomly drawn in the following ranges:

$$\begin{aligned} m_\chi &\subset [6, 15] \text{ GeV} \\ |c_{\chi 1}, c_{\chi 2}, c_{\chi 3}| &\subset [5 \times 10^{-6}, 5 \times 10^{-1}] \\ |\lambda_{ijk}| &\subset [2 C_{\phi, b, \bar{b}}, 5 \times 10^{-1}] \text{ GeV} \\ \tan\beta &= 10 \text{ and } 50, \end{aligned} \quad (23)$$

where the scan in the couplings is performed in the logarithmic scale. Note that the lower bound on the couplings λ is not a fixed number, but instead twice the coupling of any light boson to b quarks (see Eq. 5). This is to ensure that (the s-channel) annihilation dominantly proceeds into 2-body combinations of bosons a and h , the pair production of SM fermions being then suppressed and irrelevant in the computation of the relic density as well as of the indirect detection signals. This will induce a correlation between couplings λ and $C_{\chi h}$ through the range imposed on the spin-independent cross section [see Eqs. (5), (16), and (21)]. The lightest CP-even and CP-odd Higgs masses are assigned a random value, imposing the constraint $m_h + m_a \leq 2 m_\chi$ in order to guarantee that annihilation into a pair h, a is possible. We have imposed the experimental constraints on the Higgs masses and couplings as detailed in Sect. 2.3 and the condition that the singlino-proton spin-independent cross section falls within the window $\sigma_{\chi-p}^{\text{SI}} \subset [3 \times 10^{-5}, 3 \times 10^{-4}]$ pb. We have thus kept those configurations which fall in a region that contains the area compatible with the CoGeNT excess. As regards $\tan\beta$, after having tried some random scans, we have selected two extreme values only, which are sufficient to fully illustrate the impact of this parameter. In Fig. 4, we show our scan results in terms of σ^{SI} as a function of m_χ for both values of $\tan\beta$, and for two different QCD phase transition, with $T_{\text{QCD}} = 150$ and 400 MeV. The color index refers to relic density and antiproton constraints, and will be specified and discussed in Sect. 4.3. All samples we consider in the following are made of $\sim 10^5$ random models, such as those reported in Fig. 4.

To conclude this section, we must emphasize that some uncertainties in the hadronic matrix elements may affect the predictions for the direct detection rate of singlinos. The largest effect is due to the indetermination in the strange quark content of nucleons. This propagates into the theoretical predictions for the spin-independent cross section and can be responsible for a variation of about an order of magnitude [60, 61, 62, 63]. This induces an uncertainty in the values of the couplings for which the CoGeNT region can be reproduced and therefore enhances the range of these with respect to those plotted in Fig. 4. A recent illustration has been given in *e.g.* Fig. 5 of Ref. [64]. We will further discuss this issue in Sect. 4.3.2.

4. Constraints from local cosmic-ray antiprotons

Cosmic-ray antiprotons were proposed as a potential tracers of dark matter annihilation in [65]. Dark matter-induced antiprotons have been studied in the context of supersymmetry [66, 67, 68, 69, 70, 71] and extra-dimensions [72, 71], and related signals are likely very difficult to observe. Current observations by *e.g.* the PAMELA [73] or BESS [74, 75, 76, 77] experiments are in agreement with the predictions of secondary antiprotons [78, 79, 73], *i.e.* those created from nuclear interactions of standard astrophysical cosmic rays with the interstellar gas, although some models still fail to saturate the data, leaving a small room for exotic primary contributions [80, 81]. The case for light supersymmetric neutralinos was studied in [82].

Based on recent studies on cosmic-ray transport parameters [83] and on the local dark matter density [84, 85], it was

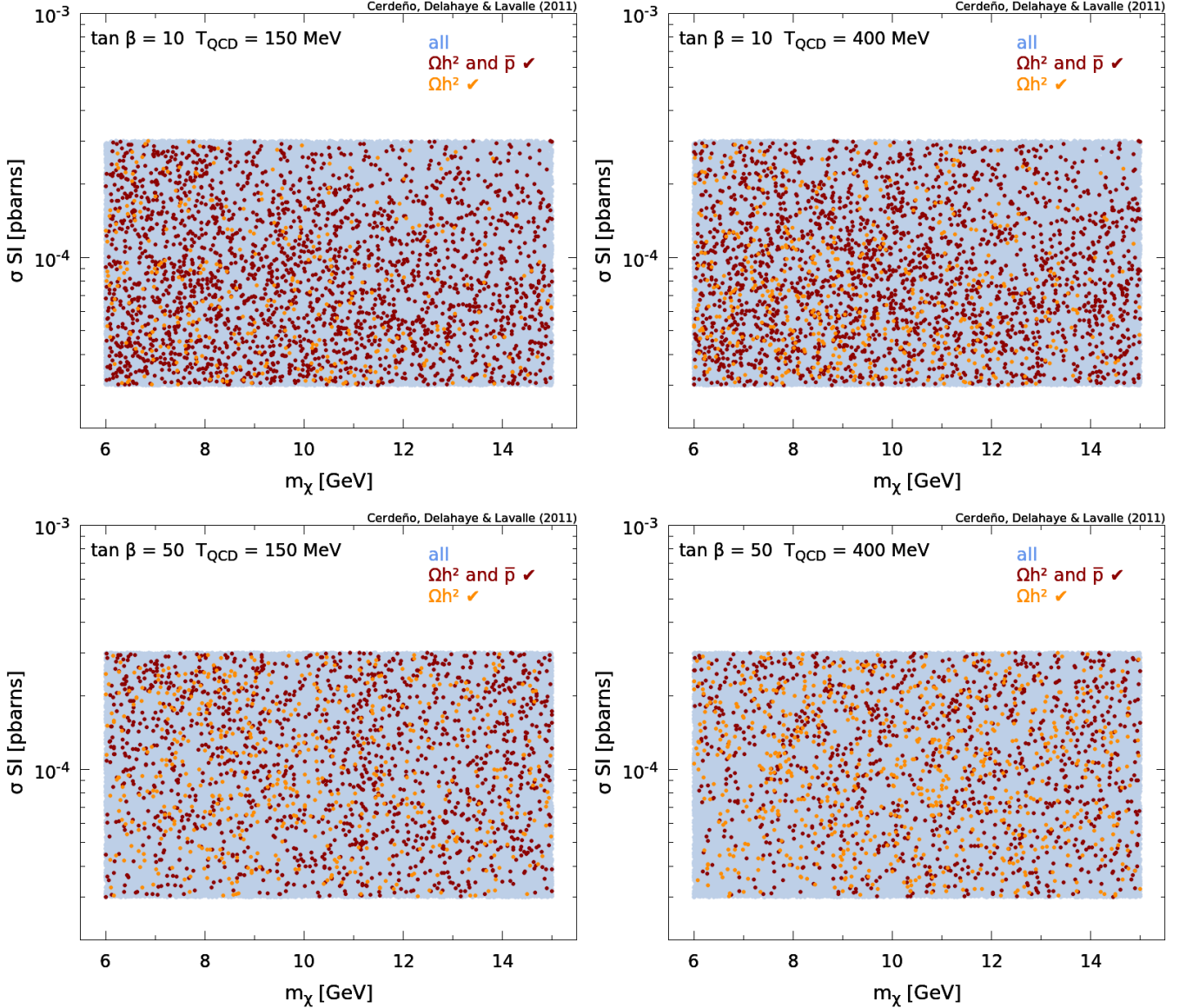


Figure 4: Spin-independent cross section as a function of the singlino mass, for different values of $\tan\beta$ — 10 (left panel) and 50 (right panel). Each panel shows $\sim 10^5$ models randomly drawn according to Eq. (23) and selected such that σ^{SI} falls in the CoGeNT region. The color index is specified in Sect. 4.3.1.

shown that ~ 10 GeV light WIMPs annihilating into quark pairs were in serious tension with the low energy cosmic-ray antiproton data [32]. In this paper, we are focusing on a quite different phenomenology where WIMPs annihilate into light scalar h and pseudo-scalar a Higgs bosons, which may further decay into quarks. These light bosons do not have necessarily the same masses, so one can for instance be more Lorentz boosted than the other. Therefore, the energy distribution of the potentially created antiprotons is expected to differ from those arising from direct annihilation into quark pairs, and the results obtained in [32] can hardly be extrapolated. In this section, we first determine the antiproton energy spectrum associated with the decay of light Higgs bosons into quark pairs before calculating the dark matter-induced flux at the Earth.

4.1. Antiproton production

Before estimating the antiproton flux at the Earth, one needs to know the antiproton spectrum before propagation, *i.e.* the one arising from the decay/hadronization of the dark matter annihilation products, here the scalar h and pseudo-scalar a . The only decay final states relevant to antiproton production are actually quark pairs energetic enough to produce a pair of proton-antiproton. This means that antiprotons can be created each time a light (pseudo-)scalar boson is heavier than twice the proton mass, roughly, which sets a production threshold to $m_\phi \gtrsim 2$ GeV.

The first step to get the antiproton spectrum is easy: before the decays of our light (pseudo-)scalars, we have a mere two-in-two-body annihilation so all the 4-momenta are set by kinematics. Assuming that dark matter particles annihilate at rest in

the Galactic halo frame, the energy of resulting particle 1 is

$$E_1 = \frac{4m_\chi^2 + m_1^2 - m_2^2}{4m_\chi} \quad (24)$$

and the norm of its momentum is

$$k_1 = \frac{\sqrt{\lambda(4m_\chi^2, m_1^2, m_2^2)}}{4m_\chi}, \quad (25)$$

where $\lambda(a^2, b^2, c^2) = (a^2 - (|b| + |c|)^2)(a^2 - (|b| - |c|)^2)$, which are enough to change from the halo frame to the rest frame of particle 1: $(\gamma, \beta) = (E_1/m_1, k_1/E_1)$. In the rest frame of particle 1, the quarks it decays into have energy $E_q^* = m_1/2$ and momentum $|k_q^*| = \sqrt{m_1^2/4 - m_q^2}$. One finally gets the energy of the quarks in the halo frame from a mere Lorentz transform:

$$\begin{aligned} E_q &= \frac{E_1}{2} - \cos(\theta) \frac{\sqrt{\lambda(4m_\chi^2, m_1^2, m_2^2)}}{8m_\chi} \sqrt{1 - \frac{4m_q^2}{m_1^2}} \\ &= \frac{E_1}{2} - \cos(\theta) \mathcal{E}. \end{aligned} \quad (26)$$

Thus, the energies of the quarks and anti-quarks coming from the decay of particle 1 are evenly distributed between $\frac{E_1}{2} - \mathcal{E}$ and $\frac{E_1}{2} + \mathcal{E}$. One finally gets the probability of having an antiproton of energy $E_{\bar{p}}$ from a quark of energy E_q $f(E_q, E_{\bar{p}})$ thanks to the PYTHIA⁴ package [86]. Eventually, the antiproton spectrum obtained after decay of the annihilation products is:

$$\mathcal{F}(E_{\bar{p}}) = \sum_{i=1,2} \sum_q \text{Br}_{i,q} \int_{\frac{E_1}{2} - \mathcal{E}}^{\frac{E_1}{2} + \mathcal{E}} \frac{f(E_q, E_{\bar{p}}) + f(E_{\bar{q}}, E_{\bar{p}})}{2\mathcal{E}} dE_q, \quad (27)$$

where the first sum is done over the annihilation products $(1,2)=(a, h)$, and the second sum is over all those quark flavors for which $2m_q \leq m_i$ is satisfied. The branching ratios $\text{Br}_{i,q}$ can be derived from the couplings to SM fermions given in Eq. (5) and the decay widths given in Eq. (6). For the quark masses, we use the pole masses reported in *e.g.* [87].

It is clear that the decay into the down-type b quark-antiquark pairs will dominate whenever permitted. When $m_i < 2m_b$, the dominant decay channel becomes $\phi_i \rightarrow \tau^+ \tau^-$ because of the more favorable dependence into $\tan\beta$ with respect to the up-type quark c . Therefore, the antiproton production is reduced in the range $2m_\tau \lesssim m_i \lesssim 2m_b$, but not completely suppressed, since d and s quark contributions remain significant. We have calculated the decay branching ratios explicitly in Fig. 5 assuming $c_\varphi = c_\theta = 0.9$ and $\tan\beta = 10$ (50) on the left (right) panel. Those associated with the third, second and first generation fermions are reported with solid, dashed, dotted lines, respectively. These curves are relevant to h and a , but we recall that we have only constrained the mixing of h so far. For simplicity, we take the same mixing angles for a , which can be considered as conservative for the antiproton production — for

example, a slight increase of the up Higgs doublet content of a would reduce the production of τ leptons.

Finally, we also consider the possibility that h decays into $2a$, a channel that is open when $m_h \geq 2m_a$. This channel is relevant when the coupling $\lambda_{aah}/m_h \gtrsim C_{\phi q \bar{q}}$ (see Eq. 6). Given the range we have considered for λ (see Eq. 23), this barely happens in our scan. Still, we note that if this channel is open and dominant, then the upper limit on the mixing parameter s_φ can be relaxed (see Sect. 2.3); for simplicity, we still do not relax it.

An illustration of the spectrum determination is presented in Fig. 6, where we have used different combinations of the masses m_χ , m_a and m_h and applied the Lorentz boost procedure described above — we did not include $h \rightarrow aa$. We have considered five different cases, with $m_\chi = 12$ GeV for each. We first see that each time $m_a, m_h > 2$ GeV, the antiproton production is rather efficient and peaks with almost the same amplitude, within a factor of ~ 3 , with a sharp decrease. The brown curve (third from top at peak energy) shows the case $m_\chi = m_a = m_h$, which means that a and h both mostly decay at rest into b quarks. Nevertheless, these quarks are created with a relatively small momentum ($E_b = m_{a,h}/2 = 6$ GeV), which reduces the proton and antiproton production efficiency. The violet (upper) curve shows a more favorable situation in which $m_a = 12$ GeV and $m_h = 4$ GeV, *i.e.* both a and h can decay into quarks with momenta large enough to fragment into antiprotons efficiently — the center of mass energy is $2m_\chi$, and the production of τ is still not strongly dominant for the h decay because very close to threshold (see Eq. 6 and Fig. 5). The pink curve (second from top) characterizes an unexpected situation where, although h and a decays dominantly into τ leptons, the remaining $\sim 30\%$ going into s and d quarks are very efficient at producing antiprotons thanks to their large momenta. The orange curve (fourth from top) shows a less favorable case for antiproton production in which a is not massive enough, and the b quarks coming from the h decay have low momenta, which translates into a factor of ~ 2 suppression with respect to the previous case. Finally, the blue (lower) curve corresponds to an even worse case, too small m_a and $m_h = 10$ GeV, where b quarks are inefficient at producing antiprotons in addition to threshold effects (the decay into τ comes into play — see Fig. 5).

These spectral differences that depend on the mass combination demonstrate that there are non-trivial ways to suppress the antiproton production, *e.g.* producing b quarks at threshold with low momenta. Nevertheless, we will further show that each time a or h can decay into antiprotons efficiently, the antiproton flux is always in tension with the current data, provided the s-wave contribution to the annihilation cross section given in Eq. (12) is dominant at freeze out.

4.2. Antiproton flux at the Earth

4.2.1. Dark matter halo

To predict the antiproton flux at the Earth, we need to specify the dark matter distribution in the Galaxy. Many conventional dark matter halo functions and related parameters have been

⁴For this work we made use of version 6.4.24 with CDF tune A.

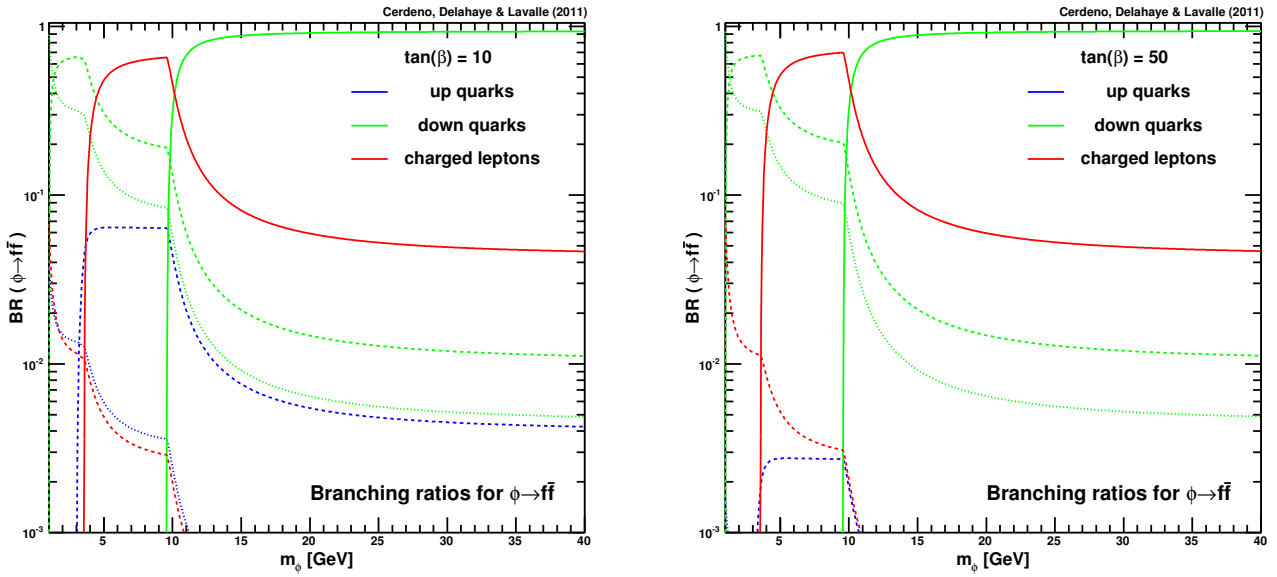


Figure 5: Branching ratios for the (pseudo-)scalar ϕ decay into SM fermions as a function of its mass m_ϕ . Contributions of the third, second and first generation fermions are reported with solid, dashed, dotted lines, respectively.

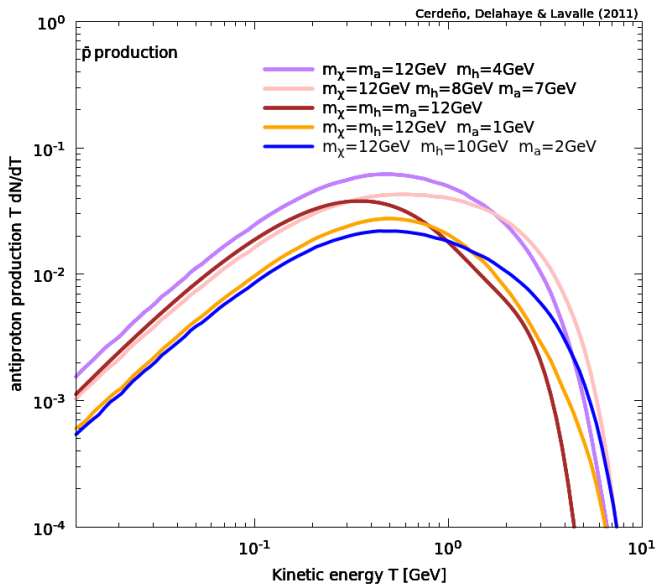


Figure 6: Antiproton energy distributions for different mass combinations.

widely used in the literature so far, but we aim at employing a distribution as constrained as possible, both theoretically and observationally. From the theoretical point of view, there seems to be a consensus in using an Navarro-Frenk-White (NFW) profile [88, 89] or an Einasto profile [90, 91], which are found to provide good fits to the dark matter distributions in cosmological N-body simulations (see *e.g.* [92]). The former is mildly cuspy in the center, behaving like r^{-1} , while the latter asymptotically flattens towards the center. Nevertheless, we stress that the very central parts of the Galaxy could differ from what most

of dark matter-only N-body simulations have predicted because baryons dominate the gravitational potential there, which might modify the central behavior of the distribution [93]. From the observational point of view, observations of low surface brightness galaxies also seem to indicate cores instead of cusps in these objects [94], showing that profiles are likely not universal in the centers. Still, in contrast to gamma-rays, the antiproton signal is well known to have almost no dependence in the distribution in the Galactic center, provided it is less cuspy than $r^{-3/2}$ [69, 79, 32]: this is due to diffusion effects. Much more important is the local dark matter density, which roughly sets the antiproton flux. It is therefore of stronger relevance to use a model dynamically constrained on kinematic data.

Recently, complementary efforts were undertaken to constrain the local density of dark matter ρ_\odot [84, 85, 95], the results of which all point to $\rho_\odot \simeq 0.4 \text{ GeV/cm}^3$. Here, we will use the spherically symmetric NFW profile as constrained in [95], which we recall hereafter:

$$\rho(r) = \rho_\odot \left[\frac{r_\odot}{r} \right] \left[\frac{1 + r_\odot/r_s}{1 + r/r_s} \right]^2, \quad (28)$$

the variable r denoting the galactocentric radius, and setting the parameters to $r_\odot = 8.28 \pm 0.16 \text{ kpc}$, $\rho_\odot = 0.40 \pm 0.04 \text{ GeV/cm}^3$ and $r_s = 18 \pm 4.3 \text{ kpc}$. We emphasize that the antiproton flux will be sensitive mostly to variations in ρ_\odot , not in the other parameters.

In principle, consistency imposes to consider dark matter substructures [96, 97], which can increase the antiproton flux at low energy [98, 99]. While the amplification is expected to be small [99], we stress that even a factor of 2 could have important consequences in delineating the antiproton constraints, as will be shown later. Here, we will not consider substructures, which can therefore be considered as a conservative approach.

K_0	δ	L	V_c	V_a
kpc ² /Myr		kpc	km/s	km/s
0.0112	0.70	4	12	52.9

Table 1: Transport parameters associated with the best-fit model of [103].

4.2.2. Antiproton transport and flux at the Earth

Once antiprotons are injected in the Galaxy, they diffuse on magnetic inhomogeneities and experience different additional processes. At low energy, say below a few GeV, they are sensitive to Galactic winds which translate into convection upwards and downwards the Galactic disk and into adiabatic energy losses; they are also sensitive to nuclear interactions with the interstellar gas, which may destroy them and/or decrease their energy; finally, they can be reaccelerated because of the proper motion of the magnetic scatterers. Higher energy antiprotons are roughly sensitive to spatial diffusion only. The general steady state equation that drives their evolution in phase-space reads:

$$\underbrace{Q(\vec{x}, E, t)}_{\text{source}} = \underbrace{-\vec{\nabla} \cdot \left\{ \left(K_{xx}(E) \vec{\nabla} - \vec{V}_c \right) \mathcal{N} \right\}}_{\text{spatial current}} \quad (29)$$

$$+ \underbrace{\partial_p \left\{ \left(\dot{p} - \frac{p}{3} \vec{\nabla} \cdot \vec{V}_c - p^2 K_{pp}(E) \partial_p \frac{1}{p^2} \right) \mathcal{N} \right\}}_{\text{current in momentum space}} + \underbrace{\Gamma_s \mathcal{N}}_{\text{spallation}}$$

where $\mathcal{N} = \mathcal{N}(\vec{x}, p) = dn/dp = \beta dn/dE$ is their differential density, K_{xx} and K_{pp} are respectively the diffusion coefficients in space and momentum, V_c is the convection velocity and $\Gamma_s = \Gamma_s(\vec{x}, p)$ the spallation rate. This equation can be solved numerically [100] or semi-analytically [101, 102, 103]. In this study, we have used the semi-analytical method sketched in *e.g.* [103, 69, 79, 98], to which we refer the reader for more details. For the transport parameters, we have utilized the best-fit model found in [103] and still in excellent agreement with more recent analyses (*e.g.* [83]). This transport model was dubbed *med* (for *median*) configuration in [69]. It is a slab transport model, with a cylindrical diffusion volume of radius $R = 20$ kpc, half-height $L = 4$ kpc, in which the diffusion coefficient obeys $K_{xx}(E) = \beta K_0 (\mathcal{R}/1 \text{ GV})^\delta$ ($\mathcal{R} = p/q$ is the cosmic-ray rigidity). The main parameters are reported in Tab. 1.

The source term is characterized by the specific dark matter model configuration:

$$Q(\vec{x}, E) = Q(r, E) = \frac{\langle \sigma v \rangle}{2} \left\{ \frac{\rho(r)}{m_\chi} \right\}^2 \frac{dN_{\text{dec}}}{dE}, \quad (30)$$

where $\langle \sigma v \rangle = a_{ah}$ is the annihilation cross section in the Galaxy given in Eq. (12), and dN_{dec}/dE is the antiproton spectrum arising from the (pseudo)-scalar decay and determined in Sect. 4.1.

Assuming a Green function $\mathcal{G}(\vec{x}, p \leftarrow \vec{x}_s, p_s)$ solution to Eq. (29), the antiproton flux at the Earth is given by the fol-

lowing expression:

$$\phi_\oplus(E) = \frac{\beta c}{4\pi} \int dp_s \int_{\text{slab}} d^3 \vec{x}_s \mathcal{G}(\vec{x}, p \leftarrow \vec{x}_s, p_s) Q(\vec{x}_s, E_s). \quad (31)$$

In practice, we use the Bessel series method presented in [69, 79], but we have checked with a couple of configurations that results obtained from Green function methods [79, 98] are equivalent.

4.3. Results and discussion

We have performed a scan over the masses and couplings associated with Eq. (1) such that we keep only those configurations falling in the so-called CoGeNT region (see Sect. 3). For these configurations, we have computed the annihilation cross section summing over the three diagrams of Fig. 2 for all possible final states, *i.e.* aa , hh and ah as soon as kinematically allowed — we recall that we have imposed $2m_\chi \geq m_a + m_h$. Then, we have derived the relic density assuming different QCD phase transition temperatures, and computed the antiproton fluxes for models leading to the correct relic abundance, *i.e.* $0.0941 \leq \Omega_\chi h^2 \leq 0.1277$ in this study (see Sect. 2.4). The flux is computed assuming the transport parameters of Tab. 1, and a solar modulation is subsequently accounted for in the force-field approximation [104, 105], with a Fisk potential of $\Phi = 600$ MV, consistent with the average solar activity during the PAMELA data taking [73]. For the secondary antiproton flux, we use the predictions obtained in [78] with the same transport parameters. It is represented in the left panel of Fig. 7 together with a prediction using another parameter set characterized by a larger diffusion halo with $L = 15$ kpc. Both predictions are consistent with the current PAMELA data [73], while the latter transport model would lead to a significantly larger primary antiproton flux because integrating over much more dark matter annihilation products. It turns out that large diffusion halo models, *i.e.* with $L \gtrsim 5$ kpc, are favored by several recent studies on Galactic cosmic-ray transport [83, 81], while small halo models with $L \lesssim 2$ are strongly disfavored from complementary observations [101, 106, 32] and are to be considered as extreme cases — we complete this discussion in Sect. 4.3.2. Therefore, we will stick to our median transport model which can be thought of as rather conservative.

We finally confront the predicted antiproton fluxes with the PAMELA data⁵. An error box is defined as having the energy bin width and the $1\text{-}\sigma$ error bar half-height. A model is considered in tension with the data when the predicted flux (adding up the primary and secondary contributions) is above an error box without crossing it⁶. A few examples are shown in the right panel of Fig. 7, where the same injected spectra as in Fig. 6 have been used as compared to the case of an annihilation into $b\bar{b}$. A conventional annihilation cross section of $\langle \sigma v \rangle = 3 \times 10^{-26} \text{ cm}^3/\text{s}$ was assumed, for which all models appear in excess with respect to the data. This clearly illustrates

⁵Other data are not considered because data taken from space are supposed to have smaller systematic errors than balloon data for a given statistics; moreover, PAMELA operated during low solar activity periods, which is optimal for low energy cosmic ray studies.

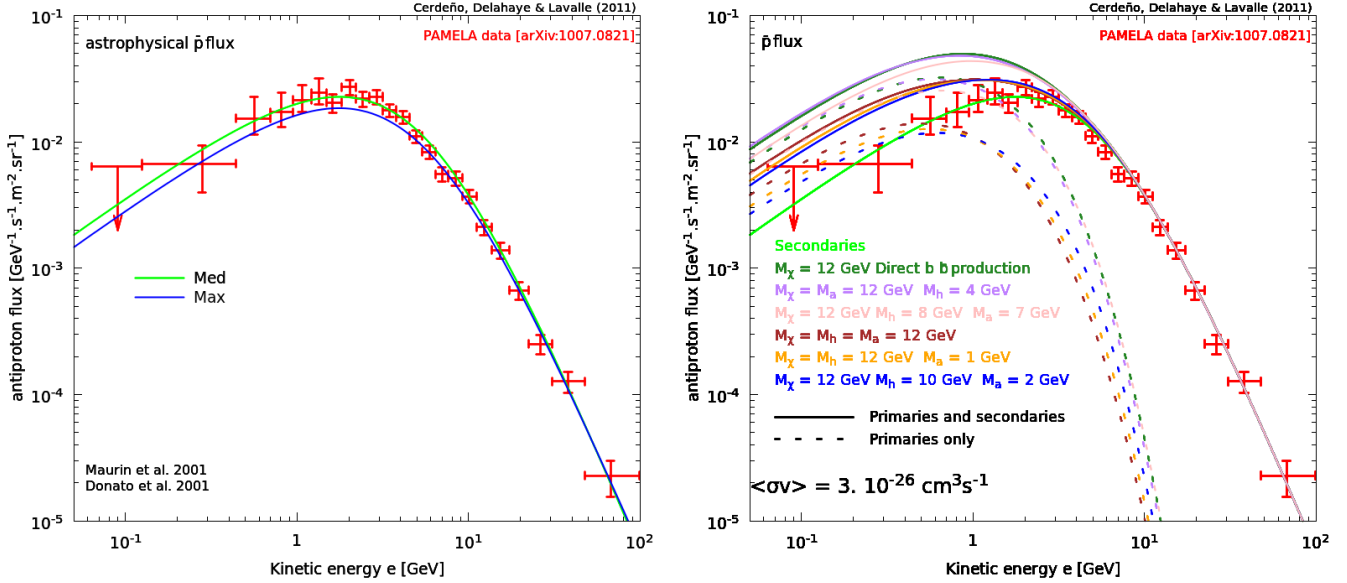


Figure 7: Left: secondary antiproton flux (background) and rough theoretical uncertainties. Right: examples of primary fluxes with the same scalar and singlino mass combinations as in Fig. 6; they are compared to a $b\bar{b}$ spectrum similar to the one used in [32].

the rejection power of the antiproton analysis. In the following we present the results we obtained from scans that cover the CoGeNT region, as detailed in Sect. 3.

4.3.1. CoGeNT region scan analysis

Fig. 4 shows the results of two scans we performed to cover the CoGeNT region in the plane $m_\chi - \sigma^{\text{SI}}$. Dark red points are those which fulfil the relic density constraint, and the light orange points are those in excess with respect to the antiproton data. Both populations can roughly cover the whole region, for small (upper panels) as well as for large values (lower panels) of $\tan\beta$, independently of T_{QCD} . Still, taking small values of $\tan\beta$ results in more cosmologically relevant configurations in average, as it can be observed. Indeed, $\tan\beta = 10$ implies a coupling $c_{\chi h}$ a factor of ~ 10 larger than in the case of $\tan\beta = 50$, for a given spin-independent cross section (see Eq. 21), which provides more room to get the correct relic density only from the annihilation into hh . Modifying the QCD phase transition temperature leaves these statements valid (see left/right panels). More generally, Fig. 4 demonstrates that we cannot draw a generic antiproton exclusion contour in this plane, since many configurations pass both the cosmological and the antiproton tests. Nevertheless, it shows that the antiproton constraints are relevant *everywhere* in this plane, which is by itself an important result. In the following, we provide details about the nature of those points which are (or not) in excess with respect to the antiproton data.

In Fig. 8, we replot the scan results of Fig. 4 in the plane $\langle\sigma v\rangle_0 - m_\chi$. Note that $\langle\sigma v\rangle_0$ refers to the annihilation cross section relevant to indirect detection, *i.e.* the velocity-independent contribution given in Eq. (12), while the full velocity-dependent

annihilation cross section was used in the relic density calculation. We remark that the relic density constraint obviously translates into an upper bound $\langle\sigma v\rangle_0 \lesssim 5(8) \times 10^{-26} \text{ cm}^3/\text{s}$ for $T_{\text{QCD}} = 150(400) \text{ MeV}$, but that the cosmologically viable points spread down to arbitrarily small values of $\langle\sigma v\rangle_0$ that correspond to cases where the P-wave is dominant, *i.e.* where annihilation proceeds mostly into hh or aa at freeze out. This demonstrates that the kinematic condition $2m_\chi \geq m_a + m_h$ does not generically ensure that annihilation into ah dominates. Indeed, suppressing the coupling between the singlino and the pseudo-scalar a is enough to suppress the S-wave, as shown in Eq. (12). We will come back to this later. The population located close to the upper cosmological bound is featured by those configurations for which annihilation is saturated by the S-wave, *i.e.* annihilation into ah . This is precisely where the antiproton constraint is the strongest. There is still a significant population that remains unaffected by the antiproton constraints in this region. This actually corresponds to cases where the decays of a and h do not produce antiprotons efficiently (see discussion in Sect. 4.1). Eventually, the impact of changing T_{QCD} is a bit harder to figure out from our scan results. Typically, considering large values of T_{QCD} implies a larger cross section at freeze out over a broader WIMP mass range, *i.e.* when $m_\chi/x_f \lesssim T_{\text{QCD}}$ (see Fig. 1). This means that going from $T_{\text{QCD}} = 150$ to 400 MeV , we increase the required annihilation cross section by a factor of ~ 2 in the singlino mass range $\sim 4\text{-}12 \text{ GeV}$ (see Fig. 1).

A way to identify the impact of the S-wave content of the annihilation cross section on the antiproton constraint strength consists in determining the S-wave to P-wave ratio, as shown in Fig. 9. Each panel illustrates the ratio a_{ah}/b_{hh} versus the ratio a_{ah}/b_{aa} for different combinations of $\tan\beta$ (10/50 on top/bottom panels) and T_{QCD} (150/400 MeV on left/right panels). The additional factor of 20 applied to the ratios comes from that we

⁶We have dismissed those data points which systematically lie below the secondary flux prediction by more than a standard deviation.

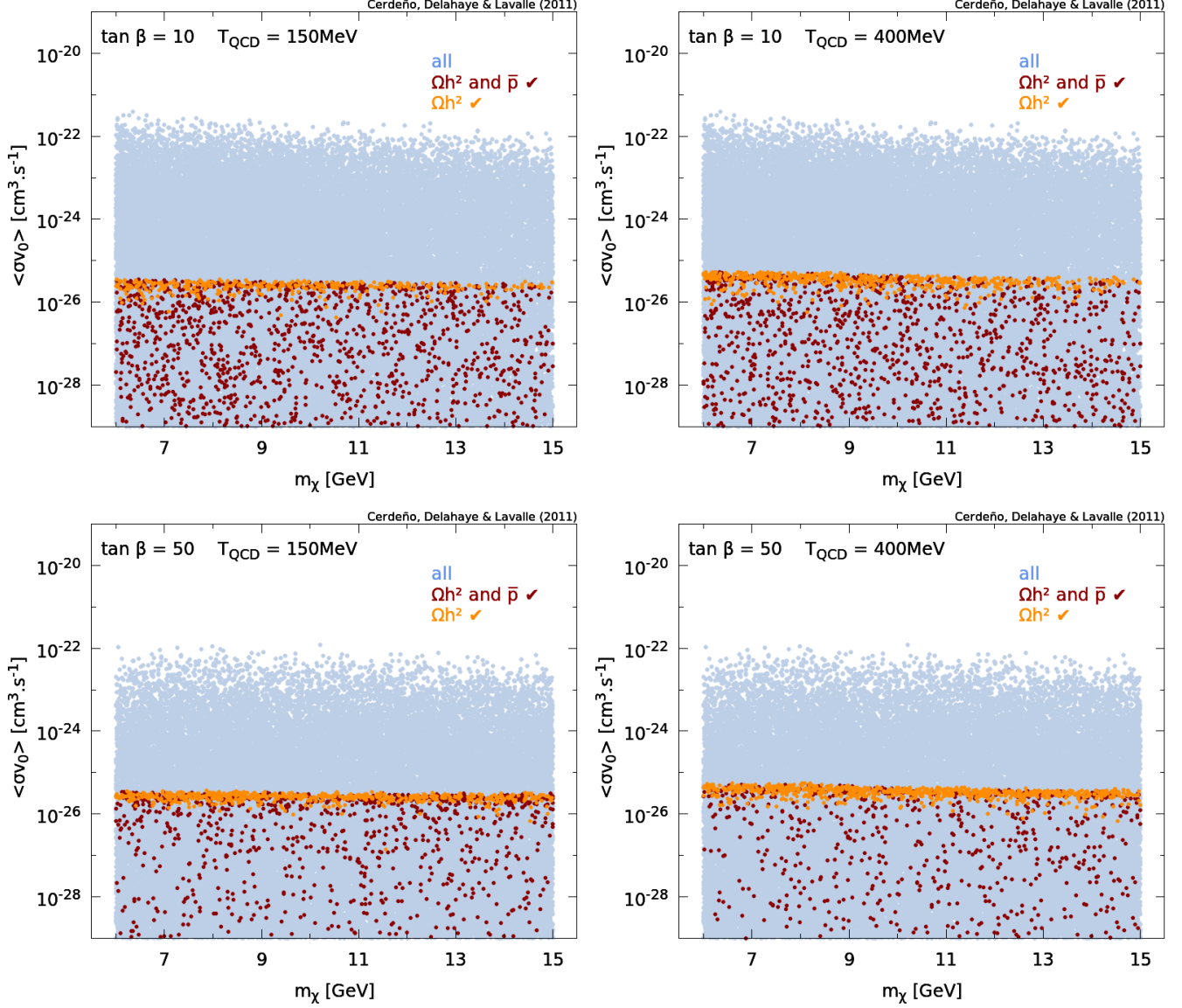


Figure 8: CoGeNT points in the plane $\langle\sigma v\rangle$ (S-wave only) versus m_χ . Top panels: $\tan\beta = 10$. Bottom panels: $\tan\beta = 50$. Left panels: $T_{\text{QCD}} = 150\text{ MeV}$. Right panels: $T_{\text{QCD}} = 400\text{ MeV}$. Dark red points are cosmologically allowed, light orange points are cosmologically allowed but lead to an antiproton excess.

want to estimate their values close to the freeze out, which occurs around $x_f = m_\chi/T \sim 20$ (see Eq. 11). Let us denote

$$\begin{aligned}
 SP_{aa} &= 20 a_{ah}/b_{aa} \\
 SP_{hh} &= 20 a_{ah}/b_{hh} \\
 SP_{\text{tot}} &= 20 a_{ah}/(b_{aa} + b_{hh}),
 \end{aligned}
 \tag{32}$$

where a_{ah} , b_{aa} , and b_{hh} are defined in Eqs. (12,13,14), respectively. In each panel of Fig. 9, going from bottom to top means decreasing the relative contribution of the annihilation into hh , while going from left to right means decreasing the relative contribution of the annihilation into aa . The top left part of each panel, where annihilation into aa is always dominant with respect to other channels, is barely populated. In contrast, there is a dense wake of points going diagonally from the bottom right part to the bottom left part, which is charac-

teristic of an annihilation driven by hh production; indeed, as long as $SP_{hh} < SP_{aa} < 1$, this channel overtops the others⁷. This implies that annihilation into aa is always subdominant in our sample. This is partly a consequence of requiring the CoGeNT region to be fulfilled, which constrains the coupling $c_{\chi h}$ to be large, while $c_{\chi a}$ is left free; besides, we see that going to larger values of $\tan\beta$ slightly alleviates this effect, as expected (see Eq. (22)). Another cause is less trivial: increasing $c_{\chi a}$ does not only increase annihilation into aa , but also that into ah (see Eq. 12); the latter is always kinematically allowed here, but not necessarily the former.

Fig. 9 further lets us distinguish a particular area, made

⁷Note that the sharp trend is reminiscent from the correlation arising between couplings λ and $C_{\chi h}$ (see Eq. 23 and discussion below); the wake would have been more spread without this correlation.

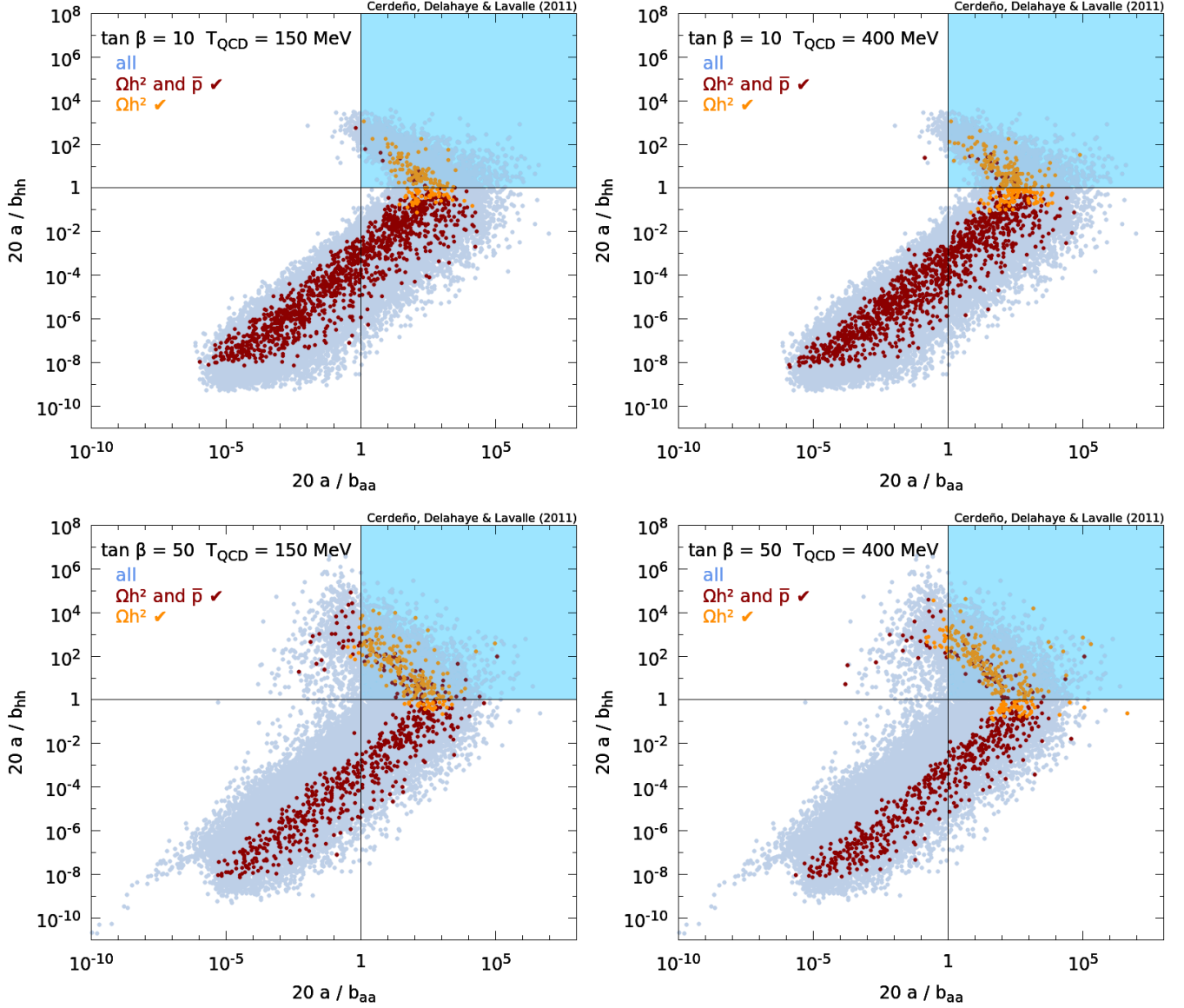


Figure 9: S-wave to P-wave ratio, a_{ah}/b_{aa} versus a_{ah}/b_{hh} , as calculated from Eqs. (12,13,14).

shaded in each panel, that corresponds to $SP_{aa} > 1$ and $SP_{hh} > 1$. This area is the region where the S-wave saturates the full annihilation cross section at freeze out, and is therefore fully fixed by the relic density (optimal case for indirect detection). Naturally, the largest fraction of the models inducing an excess in the antiproton flux (light orange points) lies in this region. Nevertheless, there are still some configurations unaffected by the antiproton constraints there, which are actually those for which a and h are too light to decay into antiprotons (through quark fragmentation), or with masses $\gtrsim 10$ GeV for which the decay into b quarks occurs at threshold and is then inefficient at producing antiprotons ($\sim [9.5, 12]$ GeV, see Sect. 4.1). In the latter case, m_χ usually takes rather large values because of our kinematical condition, which also decreases the antiproton flux (scaling like $1/m_\chi^2$). We note that the density of unconstrained configurations increases with $\tan\beta$, which comes from three ef-

fects. First, the up/down asymmetry in the branching ratio is strongly dependent in $\tan\beta$, and taking a large $\tan\beta$ increases the relative decay into τ leptons compared to that into c and s quarks (see Eq. 6 and Fig. 5). Second, a larger value of $\tan\beta$ induces an increase in m_h for a given spin-independent cross section (see Eq. 22), and either the density of points in the mass range $m_h \sim 10$ -12 GeV increases accordingly and m_χ is pushed towards larger values. Third, a larger value of $\tan\beta$ may also translate into a smaller $\chi\chi h$ coupling, leaving more room to the $h a a$ coupling to set the relic density from the s -channel (see Eq. 12 and the left diagram of Fig. 2). The consequence is that $h \rightarrow a a$ opens up when masses permit, which may further reduce the antiproton production efficiency.

In any case, the plots of Fig. 9 show that the antiproton constraints can be generically very strong whenever $SP_{aa} \gtrsim 1$ and $SP_{hh} \gtrsim 1$, as expected — one can safely use Eqs. (12,13,14) to

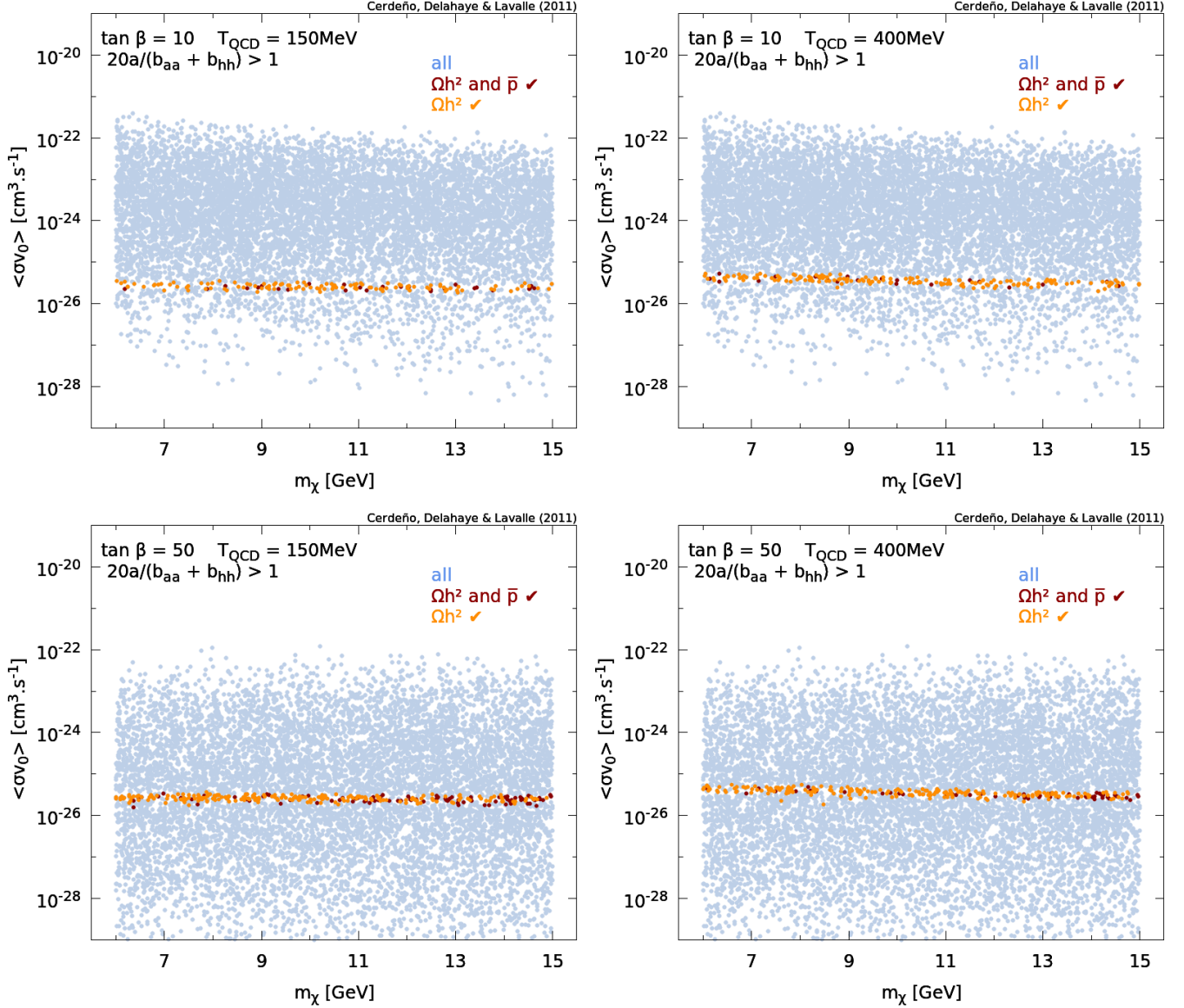


Figure 10: Same as Fig. 8 after applying the cut $SP_{\text{tot}} > 1$ (see Eq. 32).

account for this constraint.

In Fig. 10, which depicts the indirect detection annihilation cross section $\langle\sigma v\rangle_0$ as a function of the singlino mass m_χ , we report the same samples as in Fig. 8 after applying the cut $SP_{\text{tot}} > 1$ (see Eq. 32). We clearly see that this cut selects all points for which the relic density completely sets $\langle\sigma v\rangle_0$, a large fraction of which turns out to lead to an antiproton excess. The remaining unconstrained cases are mostly characterized either by $m_a \lesssim 2$ GeV, for which a cannot decay into antiprotons, or the condition $m_\chi \lesssim 10$ GeV, mostly due to the antiproton flux dependence on $1/m_\chi^2$ (see Eq. 30). This appears more clearly in the plane m_h - m_a shown in Fig. 11, where our results are presented with and without the cut $SP_{\text{tot}} > 1$ — a rectangle is drawn in each panel to emphasize the most constrained mass range. We see that once the cut is applied, all models exhibit an excess with respect to the antiproton data but those with $m_a \lesssim 2$

GeV, and $(m_a + m_h) \lesssim 20$ GeV — the latter condition is equivalent to requiring $m_\chi \lesssim 10$ GeV.

The dependence on $\tan\beta$ and T_{QCD} arises in all Figs. 8, 9, 10 and 11. Small $\tan\beta$ values are generically more constrained by the antiproton data because they lead to relatively small values of m_h for a given spin-independent cross section (see Eq. 21), thus favoring smaller values of m_χ which increases the antiproton flux. In this regime, the a/h decay into τ leptons is also slightly less significant than in the large $\tan\beta$ regime. As to the impact of T_{QCD} , things are much simpler. The cross section needs to be relatively larger for $m_\chi \lesssim 20 T_{\text{QCD}}$, which makes the indirect detection constraints more stringent for large values of T_{QCD} .

Coming back to the full results shown in Fig. 8 in the light of the previous discussion, we may summarize our results with a generic upper limit on the annihilation cross section relevant to

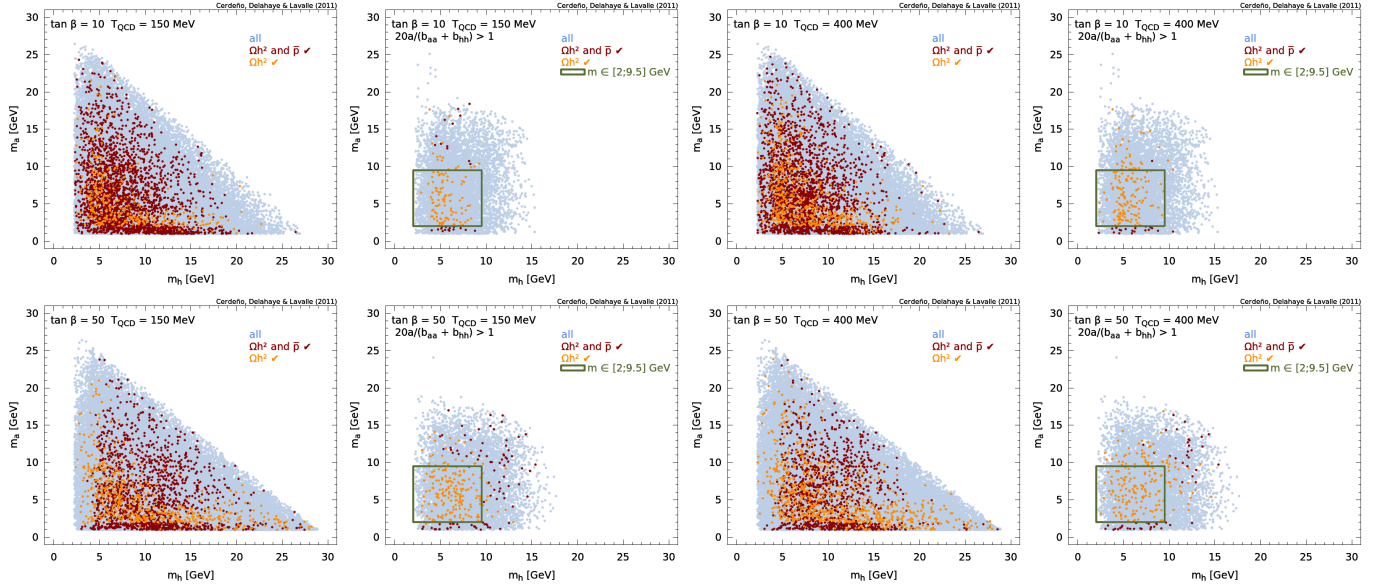


Figure 11: Scan results in the plane m_h - m_a for $\tan\beta = 10/50$ on top/bottom panels, and $T_{\text{QCD}} = 150/400$ MeV on left/right 2 columns. A cut $SP_{\text{tot}} > 1$ (see Eq. 32) was applied in the even column panels.

the singlino-like phenomenology as

$$\langle\sigma v\rangle_0 \lesssim 10^{-26} \text{ cm}^3/\text{s} \left[\frac{\rho_{\odot}/0.4 \text{ GeV}/\text{cm}^3}{m_{\chi}/10 \text{ GeV}} \right]^2 \quad (33)$$

for $\begin{cases} m_a, m_h \in [2, 9.5] \text{ GeV} \\ SP_{\text{tot}} \gtrsim 0.3 \end{cases}$.

This is not an accurate limit, but rather a way to avoid regions of the parameter space that could lead to an antiproton excess. This is illustrated in Fig. 12, where we used the worst situation for the antiproton constraints, $\tan\beta = 50$ and $T_{\text{QCD}} = 150$ MeV. We see that a looser cut of $SP_{\text{tot}} > 0.3$ still leads to an excess in the specified mass range.

Finally, we show in Fig. 13 how the antiproton constraint may translate into a constraint on the spin-independent cross section (see Eq. 21), comparing full samples (top row panels) to the same ones but after applying the cut $SP_{\text{tot}} > 1$ (middle row panels). In each top panel, the region where the relic density is set by $\chi\chi \rightarrow hh$, P-wave case irrelevant to indirect detection, covers almost the full area but the extreme right-hand side, where $\chi\chi \rightarrow ah$ becomes dominant. The (anti)correlation between $\langle\sigma v\rangle_0 \propto [\tilde{c}_{\chi\chi a}/m_{\chi}]^2$ and $\sigma^{\text{SI}} \propto [c_{\chi h}/(m_h^2 c_{\beta})]^2$ appears precisely there, which is more explicit in the middle-row panels, where the cut $SP_{\text{tot}} > 1$ was applied. From these plots, one can extract the following approximate upper limit on the direct detection phase space:

$$\left[\frac{c_{\chi h}}{c_{\beta} m_h^2} \right]^2 \approx \left[\frac{c_{\chi h} \tan\beta}{m_h^2} \right]^2 \lesssim 10^{-4} \text{ GeV}^{-4} \left[\frac{10^{-4} \text{ GeV}^{-2}}{[c_{\chi a}/m_{\chi}]^2} \right]. \quad (34)$$

In the bottom row panels of Fig. 13, we report a more explicit translation of our antiproton constraints in terms of spin-independent cross section, which can be directly compared with Fig. 4. We have applied the cut $SP_{\text{tot}} > 1$. We see that

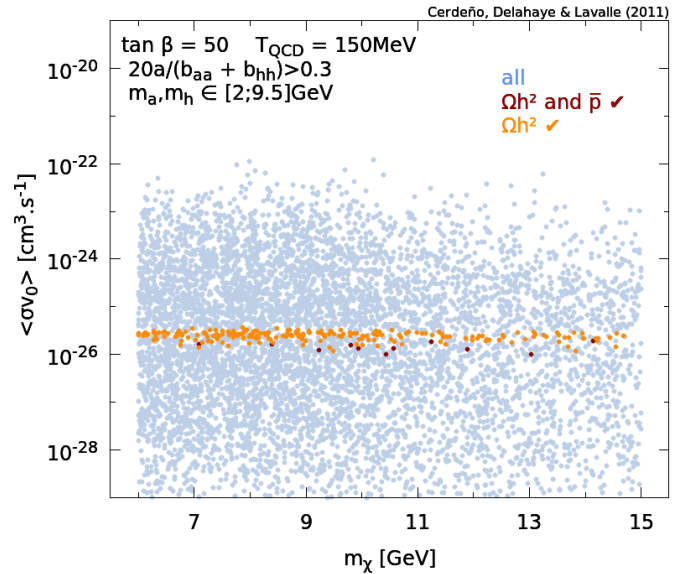


Figure 12: Example of generic antiproton constraints on singlino models. See Eq. (33).

antiprotons provide quite strong constraints for $m_{\chi} \lesssim 10$ GeV in this regime, independently of $\tan\beta$ and T_{QCD} . This nicely illustrates why the antiproton signal must be considered carefully in the singlino-like phenomenology.

4.3.2. Uncertainties and potential detection prospects for PAMELA and AMS-02

There are different sources of theoretical uncertainties that might affect our predictions. Among important effects which are related to completely different domains, some uncertainties may be connected to the QCD phase transition in the early uni-

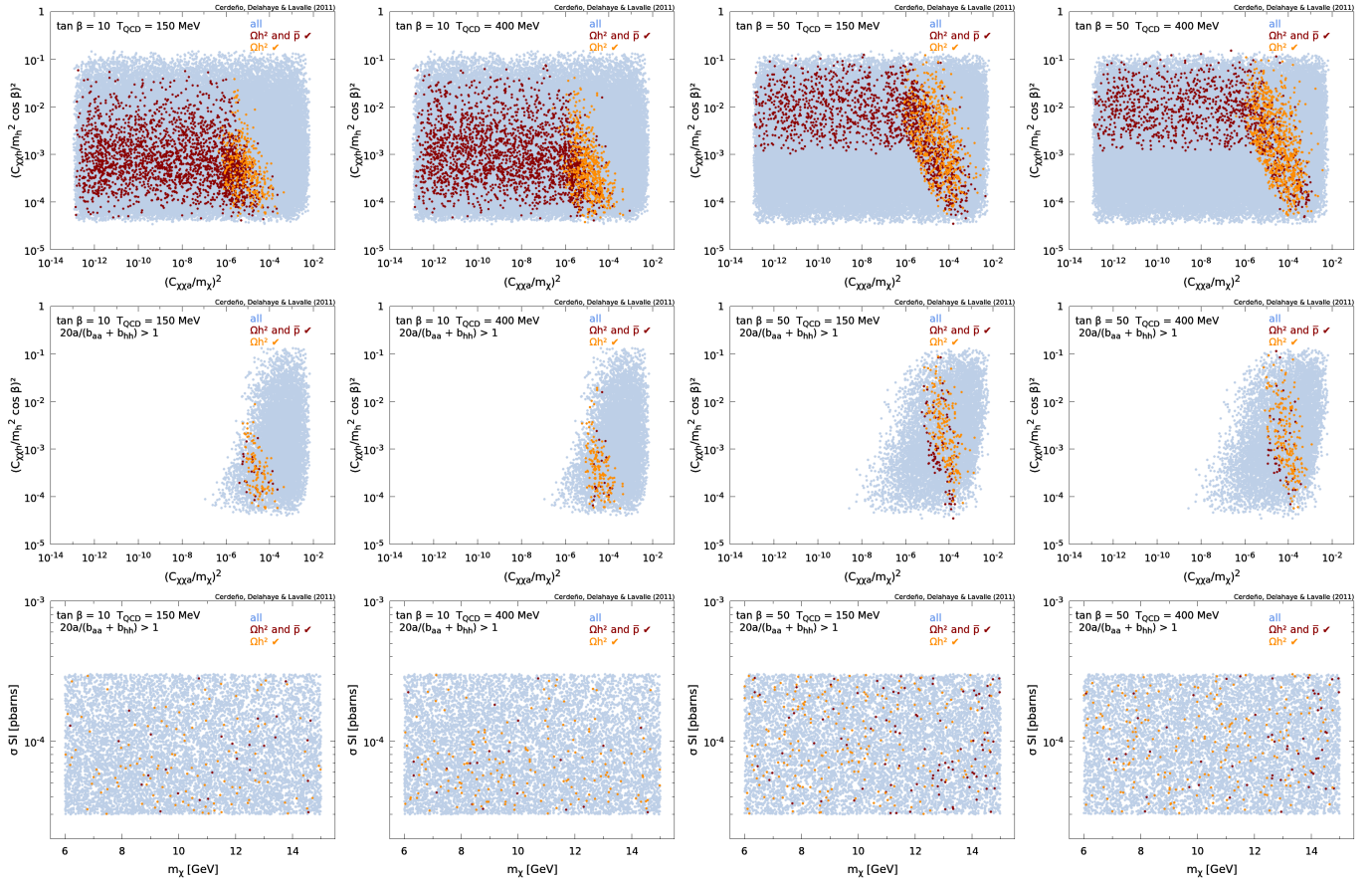


Figure 13: Potential correlation between $\langle \sigma v \rangle_0 \propto [c_{\chi a a}/m_\chi]^2$ and $\sigma^{\text{SI}} \propto [c_{\chi h}/(m_h^2 c_\beta)]^2$. Top/bottom panels: $\tan \beta = 10/50$. Left/right panels: $T_{\text{QCD}} = 150/400$ MeV. A cut $SP_{\text{tot}} > 1$ was applied to all panels.

verse (relic density), the strangeness content of nucleons (spin-independent cross section), the solar modulation modeling and the cosmic-ray transport parameters (antiproton flux).

Uncertainties in the QCD phase transition have been shown to lead to a factor of 2 uncertainty in the annihilation cross section at freeze out in the WIMP mass range $\sim 4\text{--}12$ GeV, with larger transition temperatures inducing an annihilation cross section for $m_\chi/x_f \lesssim T_{\text{QCD}}$ larger by a factor of 2 than the one obtained for $m_\chi/x_f \gtrsim T_{\text{QCD}}$, due to current constraints on the dark matter abundance (see Fig. 1). We tried to account for this uncertainty by using both a sharp QCD phase transition and two different temperatures.

Regarding uncertainties in the hadronic matrix elements, we refer the reader to Refs. [60, 61, 62, 63, 64] for more details. The consequences on our analysis are twofold, since these uncertainties can lead to select either higher (larger strangeness fraction) or smaller (smaller strangeness fraction) values of $C_{\chi h}/(c_\beta m_h^2)$ — see Eq. (22). In the former case, then annihilation into hh through the t -channel would be increased, which would likely make the population obeying $SP_{hh} < SP_{aa} < 1$ more prominent, thereby leading to a P-wave dominated annihilation cross section. This would further squeeze the configuration range available to indirect detection. Nevertheless, we point out that requiring a correct relic density poses significant constraints then, since the annihilation rate may increase too

much and lead to a too small dark matter abundance. On that account, it may become difficult to find cosmologically viable configurations, especially at small $\tan \beta$ — this is illustrated in the top panels of Fig. 13, where the upper regions are shown less favored by the relic density constraint. In contrast, the latter case, namely selecting smaller values of $C_{\chi h}/(c_\beta m_h^2)$, is more favorable to indirect detection, since a correct relic density can be achieved by means of a larger coupling $C_{\chi a}$, increasing the annihilation into ah ; so that the antiproton constraints get stronger.

Coming back to astrophysics, the low energy cosmic-ray flux below a few GeV is sensitive to the solar activity. In our calculation, the solar modulation is taken into account by using the force-field approximation [104, 105], which is known to provide a rather satisfying understanding and fit, though missing some details, of the impact of solar activity on cosmic rays [107, 108, 109]. We refer the reader to Ref. [109] for a more complete review about the current state-of-the-art. Most of the solar modulation models are based on numerical or analytical solution to the Parker transport equation [110], the force-field approximation providing an analytical solution by assuming perfect spherical symmetry and a static electromagnetic field. More complete models lead to charge sign effects depending on the solar magnetic polarity, which reverts at each 11-year solar cycle, but they are expected to be small, at the $\sim 10\text{--}20\%$

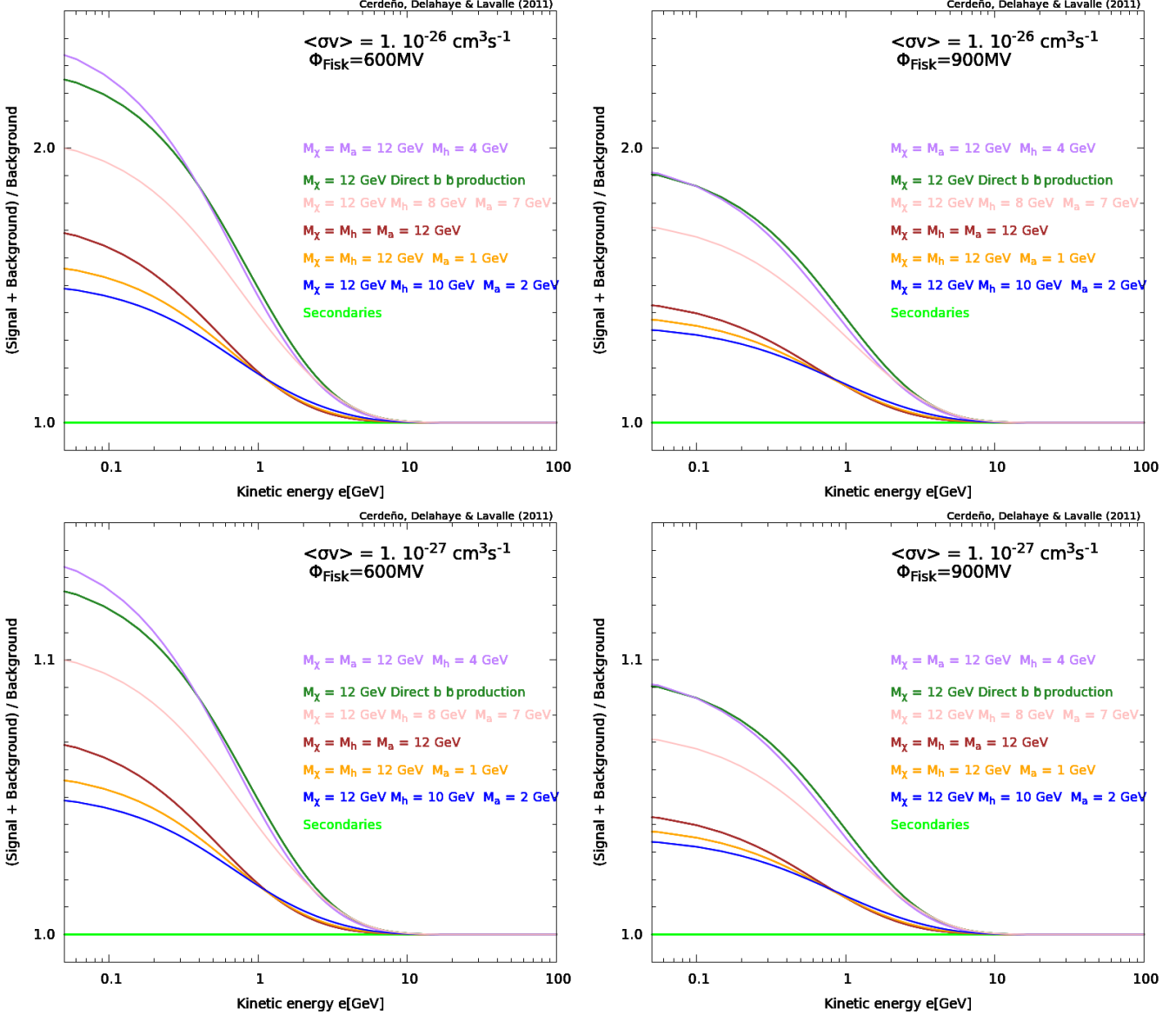


Figure 14: Signal to secondary ratio. Top: signals are computed assuming an annihilation cross section of $\langle\sigma v\rangle = 10^{-26} \text{ cm}^3/\text{s}$. Bottom: $\langle\sigma v\rangle = 10^{-27} \text{ cm}^3/\text{s}$. Left: solar modulation with a Fisk potential of $\phi = 600 \text{ MV}$. Right: $\phi = 900 \text{ MV}$.

level in terms of flux at the Earth. This roughly sizes the theoretical uncertainties affecting the force-field approximation. This has to be compared with the error bar associated with the lowest energy PAMELA data points, typically $\lesssim 1.5 \text{ GeV}$, which turn out to be the most constraining in our analysis (see Fig. 7) — the observational error is $\sim 40\%$ in this energy range, which is twice more important than the solar modulation error. We have tuned our Fisk potential to a low/intermediate value of $\phi = 600 \text{ MV}$, a rather conservative assumption with respect to the solar activity monitored during the PAMELA data taking [111]. This means that the error boxes that we have considered to derive our constraints safely encompass the theoretical uncertainty affecting the solar modulation modeling. In Fig. 14, we show the ratio of the total flux to the secondary flux, which aims at illustrating the spectral break due to additional primaries for differ-

ent amplitudes characterized by the annihilation cross section — $\langle\sigma v\rangle = 10^{-26} \text{ cm}^3/\text{s}$ ($10^{-27} \text{ cm}^3/\text{s}$) on top (bottom) panels — and for different solar activities — $\phi = 600 \text{ MV}$ (900 MV) on left (right) panels. We see that going from weak to strong solar activity can decrease a predicted excess down to $\sim 40\%$. The PAMELA data, which were taken close to a solar minimum, are therefore very well suited for to derive low energy limits.

As regards the uncertainties affecting the cosmic-ray transport parameters, we stress that one of the most sensitive parameter for dark matter-induced cosmic rays is the diffusion halo size L , which characterizes the volume which the annihilation products are integrated over and which turns out to be strongly correlated with the diffusion coefficient normalization K_0 — $K_0/L \approx \text{cst}$ from stable secondary-to-primary nuclei ra-

tio constraints like boron-to-carbon (*e.g.* [112]). Increasing L leads to integrate more annihilation products and thus increase the dark matter-induced primary flux [69, 98, 113]. In this paper, we have used $L = 4$ kpc (see Tab. 1). We emphasize that the most recent works on fitting the transport parameters tend to favor a larger diffusion zone, with $L \sim 5$ -10 kpc, which makes our propagation model rather conservative. These studies consider the additional input of the secondary radioactive cosmic ray species which allow to break the degeneracy between L and K_0 [83, 81]. Another unexpected problem in small- L diffusion zone models is that they systematically lead to a secondary positron flux in significant excess with respect to the data at low energy [114, 115]. Few other arguments in favor of larger values of L are recalled in [32] — see complementary arguments in a recent study on the diffuse Galactic radio emission [116]. Our values for K_0 and L can therefore be considered as quite motivated and rather conservative.

Finally, it is interesting to make some prospects for the end of the PAMELA campaign or the new operating space experiment AMS-02⁸, which was successfully launched in May 2011 and which is supposed to take data for $\gtrsim 10$ years. For the latter, it is not yet clear whether the low energy systematic errors can be reduced with respect to PAMELA, but statistics will for sure be much better. Fig. 14 shows how a finer PAMELA/AMS-02 data analysis could improve our current limits or lead to the detection of those singlino configurations which still induce cosmic antiprotons, but with a flux too weak to be detected or constrained. This typically corresponds to an annihilation cross section $\langle\sigma v\rangle \lesssim 5 \times 10^{-27} \text{ cm}^3/\text{s}$. We see in the bottom panels that a precision of $\sim 5\%$ makes the data quite relevant to such a low annihilation cross section, even in the case of strong solar activity. Therefore, if the PAMELA or AMS-02 collaborations manage to reach such a low precision, we expect much tighter constraints on light dark matter models annihilating into antiprotons in the future, even if the solar activity is also expected to increase in the coming years. In particular, much deeper phase-space regions with $SP_{\text{tot}} \lesssim 0.1$ (see Eq. 32) could be probed.

4.3.3. Connecting this effective approach to more constrained particle phenomenologies

The question may arise of how to connect this effective approach to existing and more constrained particle phenomenologies beyond the SM.

First, an interesting and very general link can be made by focusing on the kinematics of the final states. Indeed, we have considered that annihilation proceeds into two bodies that may further decay into quarks, leading to the production of antiprotons. We have shown that each time the annihilation cross section is S-wave dominated, then this kinematical configuration may lead to an antiproton excess quite generically. Our effective approach is therefore fully relevant to cases for which such two-exotic-body production is predicted, as in *e.g.* Ref. [117], where the so-called DAMA/CoGeNT signal is explained from

a model incorporating two additional light gauge bosons that dark matter can annihilate into. Since one of these gauge fields has a mass larger than 2 GeV, it can in principle decay into an antiproton. This model can therefore suffer the antiproton constraints. Our constraints may also be important for completely different models, like in the recent study performed in [118] of a light right-handed sneutrino dark matter that can arise in the frame of the NMSSM; annihilation can then indeed go into light pseudo-scalars without being velocity suppressed, while this case is not necessarily adapted to fit the CoGeNT region.

Given our effective Lagrangian of Eq. (1), a natural link can be made with singlet extensions of the MSSM, which was the original motivation for this work. This includes general extensions as well as more constrained ones, like for instance the NMSSM, in which the dark matter candidate is a singlino-dominated neutralino. An example of a model of singlino dark matter can be found in Ref. [23], where the specific annihilation into light (pseudo)scalar Higgs bosons is considered. Their case (3), which corresponds to $2m_\chi > m_a + m_h$, can be directly compared with our analysis. In this specific configuration, they find $|C_{\chi h}| \approx |C_{\chi a}| \lesssim |\lambda_{ijk}|$, with $|\lambda_{hhh}| \gtrsim |\lambda_{aah}|$. Having similar couplings between $\chi\chi a$ and $\chi\chi h$ implies that they both have to be large to explain the DAMA/CoGeNT signal, which also implies that the S-wave contribution of the t -channel annihilation diagram into ah is always significant. The fact that $|\lambda_{hhh}| \gtrsim |\lambda_{aah}|$ induces a competition with the s -channel annihilation into hh (P-wave), but more suppressed than the t -channel annihilation into ah (velocity suppression, and a squared propagator factor of $\sim 1/(4m_\chi^2 - m_h^2)^2$ as compared with $\sim 1/m_\chi^4$ for the t -channel). The antiproton limit must therefore be regarded in this case.

For comparisons with the NMSSM, we may use Refs. [22, 119, 120, 121]. Although the reason is not clear from the mass matrix elements only [25], it appears to be difficult to generically find viable NMSSM configurations obeying $2m_\chi > m_a + m_h$. Bosons a and h can be found very light, but not simultaneously [119, 120, 121] — an exception can be found in Ref. [22], but the authors get an annihilation going dominantly into $f\bar{f}$. The above cited studies still find complementary viable regions in the NMSSM parameter space. When the relic density is set from the s -channel resonant exchange of a light h , then the annihilation is P-wave dominated and indirect detection fails to yield interesting bounds. If, in contrast, the main annihilation final state consists in an S-wave production of quarks (even if not with a branching ratio of 1), then an antiproton excess very likely follows in most of cases — this may also happen for a right-handed sneutrino dark matter within the NMSSM [118]. This situation was already discussed in Ref. [32], where the antiproton limit was shown to be very sharp.

5. Conclusion

In this paper, we have designed a generic effective Lagrangian to survey the light singlino dark matter phenomenology, as soon as annihilation mostly proceeds into light singlet-dominated scalar h and/or pseudo-scalar a Higgs bosons

⁸<http://www.ams02.org/>

(see Sect. 2). Within this general framework, we have computed the annihilation cross section (Sect. 2.5), the relic density (Sect. 2.4), the spin-independent nucleon-singlino cross section (Sect. 3), the antiproton spectra arising from the decays of these light (pseudo-)scalar bosons (Sect. 4.1), and the subsequent antiproton flux at the Earth (Sect. 4.2.2). We have focused on a specific mass configuration that guarantees the existence of an S-wave contribution to the annihilation cross section, ensuring the relevance of indirect detection, *i.e.* $2m_\chi \geq m_a + m_h$. We then have selected the mass and coupling parameter space to get a spin-independent cross section range encompassing the so-called CoGeNT region, and drawn several samples of $\sim 10^5$ models for two different values of $\tan\beta$, 10 and 50, for which we have calculated the relic density. Then, we have computed the antiproton fluxes associated with these configurations and compared them to the PAMELA data (Sect. 4.3).

We emphasize that there are still theoretical uncertainties affecting the estimate of the annihilation cross section at freeze out for ~ 10 GeV mass WIMPs, up to a factor of ~ 2 depending on whether WIMPs decouple after or before the QCD phase transition. This is due to the rapid change in the relativistic degrees of freedom that occurs at that time and acts as a weight on the annihilation cross section. We have taken this uncertainty into account by considering extreme cases, as illustrated in Fig. 1.

Our results demonstrate (Sect. 4.3) that the antiproton constraint is generically relevant to the whole CoGeNT region (see Fig. 4), though there are some simple ways to escape it. The most trivial way to suppress the S-wave contribution to the annihilation cross section is to suppress the coupling between the singlino and the light pseudo-scalar $c_{\chi a}$, as shown by Eq. (12). Another way is to have the light scalar and pseudo-scalar Higgs bosons so light that they cannot decay into antiprotons, or cannot generate antiprotons energetic enough to be observed. Anyway, we have shown that as soon as the S-wave is significant at freeze out, the antiproton signal is in most of the cases in excess with respect to the PAMELA data (see Fig. 8, which translates into Fig. 10 after imposing the S-to-P wave ratio to be larger than 1). Depending on the singlino/scalars mass configuration, we have derived a quite generic upper limit on the annihilation cross section lying in the range $\langle\sigma v\rangle_0 \lesssim 10^{-26} \text{ cm}^3/\text{s}$, valid for the singlino mass range $\sim 6\text{-}15$ GeV. This limit is very competitive with respect to those obtained from gamma-rays [30], and complementary to limits coming from high-energy neutrinos from the Sun [31]. We recall that the antiproton bounds are even more stringent for direct annihilation into quarks (see Fig. 7 and [32]).

Uncertainties affecting our analysis have been discussed in Sect. 4.3.2, where we have shown that our procedure is to be considered as rather conservative. In addition to the points raised there, we remind that our antiproton flux calculation is poorly sensitive to the details of the dark matter distribution far away from the Earth, in contrast with the calculation of the gamma-ray flux. The main parameter which sets the flux amplitude is the local density ρ_\odot , so one can easily rescale our results and limits by a mere factor of $(\rho_\odot^{\text{new}}/\rho_\odot)^2$. Still, we recall that we have considered a dynamically constrained profile,

and that we did not include any substructure. Although their survival against tidal effects and encounters with baryonic systems (stars and/or Galactic disk) still needs to be clarified, the survival fraction is expected to be larger and larger for smaller and smaller substructures, which are more concentrated [122]. Self-consistency would then require to include their effect in our calculation [97], which turns out to be a slight increase of the antiproton flux at low energy [98, 99]. This would therefore make our present constraints even more stringent.

Finally, we have shown that provided systematic errors can be reduced down to $\sim 5\%$, PAMELA, from an improved analysis, or AMS-02 could have the capability of detecting a still unseen signal characterized by a spectral break (see Fig. 14) which would hide just within the current PAMELA error boxes we have considered in this paper. A null detection with better errors would in any case significantly ameliorate the limits derived in this paper.

Acknowledgements: *We are grateful to Gilbert Moulta for inspiring and early discussions about effective Lagrangians, and to Pierre Salati for interesting comments about the relic density calculation. We also thank Geneviève Bélanger, Fawzi Boudjema and Alexander Pukhov for helping us compare our relic density calculation results with MicrOMEGAS, and Cyril Hugonie for providing us with useful technical details about the NMSSM. D.G.C. is supported by the Ramón y Cajal program of the Spanish MICINN. This work was supported by the Spanish MICINN's Consolider-Ingenio 2010 Programme under grants MultiDark CSD2009-00064 and CPAN CSD2007-00042. We also thank the support of the MICINN under grant FPA2009-08958, the Community of Madrid under grant HEP-HACOS S2009/ESP-1473, and the European Union under the Marie Curie-ITN program PITN-GA-2009-237920.*

Appendix A. Annihilation cross section

In this appendix, we summarize our calculations of the annihilation cross section and of the relic density for pedagogical purposes (mostly dedicated to those who wish to revisit the case without any formal calculation software). The scattering amplitudes associated with the process $\chi(p_1)\chi(p_2) \rightarrow \phi_i(k_i)\phi_j(k_j)$ and consistent with the Lagrangian of Eq. (1), the Feynman diagrams of which are shown in Fig. 2, are the following (for the s, t and u channels, respectively):

$$\mathcal{M}_s = \frac{\lambda_{ijk}}{s - m_k^2 + i\Gamma_k m_k} \bar{v}(p_2) C_{\chi k} u(p_1) \quad (\text{A.1a})$$

$$\mathcal{M}_t = \frac{1}{t - m_\chi^2} \bar{v}(p_2) C_{\chi j} (\not{q}_t + m_\chi) C_{\chi i} u(p_1) \quad (\text{A.1b})$$

$$\mathcal{M}_u = \frac{1}{u - m_\chi^2} \bar{v}(p_2) C_{\chi i} (\not{q}_u + m_\chi) C_{\chi j} u(p_1), \quad (\text{A.1c})$$

where the couplings λ and C are defined in Eqs. (1) and (2)⁹, s , t and u are the Mandelstam variables and q_t and q_u the related 4-momenta:

$$s \equiv (p_1 + p_2)^2 = (k_i + k_j)^2; \quad t \equiv q_t^2; \quad u \equiv q_u^2; \quad (\text{A.2a})$$

$$q_t \equiv p_1 - k_i = k_j - p_2; \quad q_u \equiv p_1 - k_j = k_i - p_2 \quad (\text{A.2b})$$

We also introduce the functions $g(s)$ and $h(s)$ such that in the center of mass system:

$$t = m_\chi^2 - g(s) + h(s) \cos(\theta); \quad (\text{A.3a})$$

$$u = m_\chi^2 - g(s) - h(s) \cos(\theta); \quad (\text{A.3b})$$

$$\text{with } g(s) \equiv (s - m_i^2 - m_j^2)/2; \quad (\text{A.3c})$$

$$h(s) \equiv \frac{f_{ij}}{2} \sqrt{s(s - 4m_\chi^2)}, \quad (\text{A.3d})$$

where $f_{ij}(s)$ is further defined in Eq. (A.5), and θ is the angle between \vec{p}_1 and \vec{k}_i in the center of mass frame.

The differential annihilation cross section is given by:

$$d\sigma_{12 \rightarrow ij} = \frac{d\text{LIPS}}{4 E_1 E_2 \beta_{12}} \left[\frac{1}{g_\chi^2 S_{ij}} \sum_{\text{d.o.f}} |\mathcal{M}|^2 \right] \quad (\text{A.4})$$

$$\text{with } \beta_{kl} \equiv \sqrt{(p_k \cdot p_l)^2 - m_k^2 m_l^2 / (E_k E_l)},$$

where g_χ is the number of degrees of freedom of particle χ ($g_\chi = 2$ here), $S_{ij} \equiv 1 + \delta_{ij}$ is a symmetry factor, and where the integrated Lorentz invariant phase space factor reads:

$$\int d\text{LIPS} = \int \frac{d^3 \vec{k}_i}{(2\pi)^3 2E_i} \frac{d^3 \vec{k}_j}{(2\pi)^3 2E_j} \quad (\text{A.5a})$$

$$\times (2\pi)^4 \delta^4(p_1 + p_2 - k_i - k_j)$$

$$= \frac{f_{ij}(s)}{16\pi} \int_{-1}^1 dz$$

$$\text{with } f_{ij}(s) \equiv \left\{ \left[1 - \frac{(m_i - m_j)^2}{s} \right] \left[1 - \frac{(m_i + m_j)^2}{s} \right] \right\}^{1/2}. \quad (\text{A.5b})$$

Note that $z \equiv \cos(\theta)$.

To compute the temperature-averaged annihilation cross section $\langle \sigma v \rangle$, we need to express the velocity v , which is not the relative velocity $v_r/c \equiv c |\vec{p}_1/E_1 - \vec{p}_2/E_2| = \sqrt{\beta_{12}^2 + c^4 (\vec{p}_1/E_1 \times \vec{p}_2/E_2)^2}$, but the Møller velocity $v/c \equiv \beta_{12}$ [44, 46]. Incidentally, it is useful to note that $(E_1 E_2 \sigma v)$ is Lorentz invariant. Now, let us express the cross section in terms of a sum of the different contributions (s-, t-, u-channels and interferences), for a deeper understanding:

$$\sigma_{12} \beta_{12} = \sigma_{12} \beta_{12}|_s + \sigma_{12} \beta_{12}|_t + \sigma_{12} \beta_{12}|_u + \sigma_{12} \beta_{12}|_{st} + \sigma_{12} \beta_{12}|_{su} + \sigma_{12} \beta_{12}|_{tu}. \quad (\text{A.6})$$

We are armed enough to derive the cross section in the most general case, *i.e.* we can take particles $\phi_{i,j,k}$ having all a scalar

⁹We stress that this general writing introduces non-physical degrees of freedom when going to the total squared amplitude, notably for the interference terms (mixing of two different final states, *e.g.* scalar–scalar with pseudo-scalar–scalar). One has to remember that interaction terms involving $c_{\chi i} \times \tilde{c}_{\chi i}$ are forbidden — this is clear from the Lagrangian of Eq. (1) — and can therefore be dropped. As a more general rule, one can replace $c_{\chi i} \times \tilde{c}_{\chi j} \rightarrow c_{\chi i} \times \tilde{c}_{\chi j} (1 - \delta_{ij})$. Despite this caution, which is relevant when trying to give physical interpretations to the general-case result, such a general approach proves powerful since a single expression can be used for different annihilation final states; one has just to switch the appropriate couplings on/off to get the selected one, which automatically removes the unphysical terms.

and a pseudo-scalar component; we will take care of removing the non-physical degrees of freedom at the end⁹. Denoting $\sigma \beta = \sigma_{12} \beta_{12}$ and using $g = g(s)$ and $h = h(s)$, we find:

$$\sigma \beta|_s = \frac{K \lambda_{ijk}^2 \left[c_{\chi k}^2 (s - 4m_\chi^2) + \tilde{c}_{\chi k}^2 s \right]}{(s - m_k^2)^2 + \Gamma_k^2 m_k^2} \quad (\text{A.7a})$$

$$\sigma \beta|_t = \frac{K \left[g^2 - h^2 \right]^{-1}}{2} \times \quad (\text{A.7b})$$

$$\left\{ \alpha_{0t} + g \left[\alpha_{1t} + 2\alpha_{2t} g \right] - \alpha_{2t} h^2 - \frac{1}{2h} \left[\alpha_{1t} + 2\alpha_{2t} g \right] \left[g^2 - h^2 \right] \ln \left[\frac{g+h}{g-h} \right] \right\}$$

$$\sigma \beta|_u = \sigma \beta|_t \quad (\text{A.7c})$$

with $\alpha_{mt} \rightarrow (-1)^m \alpha_{mt}$; and index $i \leftrightarrow$ index j for odd m

$$\sigma \beta|_{st} = \frac{1}{4} \frac{K \lambda_{ijk} (s - m_k^2)}{(s - m_k^2)^2 + \Gamma_k^2 m_k^2} \times \quad (\text{A.7d})$$

$$\left\{ 2\alpha_{1st} - \frac{1}{h} (\alpha_{0st} + \alpha_{1st} g) \ln \left[\frac{g+h}{g-h} \right] \right\}$$

$$\sigma \beta|_{su} = \sigma \beta|_{st} \quad (\text{A.7e})$$

with $\alpha_{mst} \rightarrow (-1)^m \alpha_{mst}$; and index $i \leftrightarrow$ index j

$$\sigma \beta|_{tu} = -\frac{K}{4} \times \quad (\text{A.7f})$$

$$\left\{ 2\alpha_{2tu} - \frac{1}{gh} (\alpha_{0tu} + \alpha_{2tu} g^2) \ln \left[\frac{g+h}{g-h} \right] \right\}.$$

Parameter K , which carries dimensions of inverse squared mass, is defined as

$$K \equiv K(s) = \frac{f_{ij}(s)}{64 \pi E_1 E_2 S_{ij}}. \quad (\text{A.8})$$

The coefficients α are associated with the numerators of terms involving the t- or u-channel, which all exhibit an angular dependence. This angular dependence can be expressed as a polynomial function of z reading $P_x(z) = \sum_n \alpha_{nx} [h(s) \times z]^n$. These coefficients are explicitly given below:

$$\alpha_{0t} \equiv 2 \left\{ c_{i+}^2 c_{j+}^2 (g^2 - m_i^2 m_j^2) + \quad (\text{A.9a}) \right.$$

$$4m_\chi^2 \left[\tilde{c}_{\chi i}^2 c_{\chi j}^2 m_i^2 + \right.$$

$$\left. c_{\chi i}^2 (c_{\chi j}^2 (s - 4m_\chi^2) + \tilde{c}_{\chi j}^2 m_j^2) \right\}$$

$$\alpha_{1t} \equiv -16 m_\chi^2 c_{\chi i}^2 c_{\chi j}^2 \quad (\text{A.9b})$$

$$\alpha_{2t} \equiv -2 c_{i+}^2 c_{j+}^2, \quad (\text{A.9c})$$

$$\alpha_{0st} \equiv 8m_\chi \left\{ c_{\chi i} (c_{\chi j} c_{\chi k} (s - 4m_\chi^2) + \tilde{c}_{\chi j} \tilde{c}_{\chi k} s) - \quad (\text{A.10a}) \right.$$

$$\left. \tilde{c}_{\chi k} c_{ij-}^2 (g + m_i^2) \right\}$$

$$\alpha_{1st} \equiv -8 c_{\chi k} c_{ij+}^2 m_\chi, \quad (\text{A.10b})$$

$$\begin{aligned}\alpha_{0tu} &\equiv 16 m_\chi^2 \left[c_{\chi i}^2 \left(c_{\chi j}^2 (s - 4 m_\chi^2) + \tilde{c}_{\chi j}^2 m_j^2 \right) + \tilde{c}_{\chi i}^2 c_{\chi j}^2 m_i^2 \right] \\ \alpha_{1tu} &\equiv 0 \\ \alpha_{2tu} &\equiv 4 \left(\left[\tilde{c}_{ij+}^2 \right]^2 - \left[c_{ij-}^2 \right]^2 \right),\end{aligned}\quad (\text{A.11a})$$

$$\alpha_{2tu} \equiv 4 \left(\left[\tilde{c}_{ij+}^2 \right]^2 - \left[c_{ij-}^2 \right]^2 \right), \quad (\text{A.11b})$$

where we have used:

$$c_{l\pm}^2 \equiv c_{\chi l}^2 \pm \tilde{c}_{\chi l}^2 \quad (\text{A.12a})$$

$$c_{lk\pm}^2 \equiv c_{\chi l} c_{\chi k} \pm \tilde{c}_{\chi l} \tilde{c}_{\chi k} \quad (\text{A.12b})$$

$$c_{l/jk\pm}^2 \equiv c_{\chi l} \tilde{c}_{\chi k} \pm \tilde{c}_{\chi l} c_{\chi k}. \quad (\text{A.12c})$$

The null-velocity limit of the annihilation cross section corresponds to requiring $s \rightarrow 4 m_\chi^2$. This implies that function $h(s) \rightarrow 0$, which *a posteriori* justifies the form of Eq. (A.7), from which the full limit can be readily calculated. In terms of the above α coefficients (we now denote them $\bar{\alpha}$ to make explicit that they also have to be taken in the limit $s \rightarrow 4 m_\chi^2$), we obtain the following suitable expressions:

$$\sigma \beta|_{s,0} \rightarrow \frac{4 m_\chi^2 K \lambda_{ijk}^2 \tilde{c}_{\chi k}^2}{(4 m_\chi^2 - m_k^2)^2 + \Gamma_k^2 m_k^2} \quad (\text{A.13a})$$

$$\sigma \beta|_{t+u+tu,0} \rightarrow \frac{K [\bar{\alpha}_{0t} + \bar{\alpha}_{0u} + \bar{\alpha}_{0tu}]}{2 g^2 (4 m_\chi^2)} \quad (\text{A.13b})$$

$$\sigma \beta|_{st+su,0} \rightarrow -\frac{K \lambda_{ijk} [\bar{\alpha}_{0st} + \bar{\alpha}_{0su}] (4 m_\chi^2 - m_k^2)}{2 g (4 m_\chi^2) \left((4 m_\chi^2 - m_k^2)^2 + \Gamma_k^2 m_k^2 \right)}. \quad (\text{A.13c})$$

The above expressions are the ones which are relevant to indirect detection. We note that for the s-channel, only the pseudo-scalar exchange gives a non-zero contribution, as expected. It is also easy to check from these expressions that only annihilation into a scalar and a pseudo-scalar is non-zero in the null velocity limit.

To get the Taylor expansion terms of the thermally averaged cross section of Eq. (11), we refer the reader to Ref. [44]. Defining the Lorentz invariant function

$$W(s) = 4 E_1 E_2 \sigma \beta \quad (\text{A.14})$$

e.g. from Eq. (A.4), one can demonstrate that:

$$a = \frac{W(s)}{4 m_\chi^2} \Big|_{s \rightarrow 4 m_\chi^2} = \sigma \beta|_0 \quad (\text{A.15})$$

$$b = -\frac{3}{8 m_\chi^2} \left[2 W(s) - 4 m_\chi^2 \frac{dW(s)}{ds} \right] \Big|_{s \rightarrow 4 m_\chi^2}.$$

The zeroth order term a (often called S-wave, though it is only a part of it) is therefore fully determined by Eq. (A.13), while the first order term b requires a bit more of algebra. The latter case is left to the patience of the reader, though explicit results are given for the cases of $\chi\chi \rightarrow hh$ and $\chi\chi \rightarrow aa$ in Eqs. (13) and (14), respectively. For the indirect detection signal, we have used the analytical expression obtained for the S-wave, while for the relic density calculation we have computed the thermal average numerically following Refs. [46, 47]. We

recall the full form of the thermally averaged annihilation cross section below:

$$\langle \sigma v \rangle = \frac{\int \frac{d^3 \vec{p}_1}{2 E_1 (2\pi)^3} \frac{d^3 \vec{p}_2}{2 E_2 (2\pi)^3} f_\chi(\vec{p}_1) f_\chi(\vec{p}_2) W(s)}{\int \frac{d^3 \vec{p}_1}{(2\pi)^3} \frac{d^3 \vec{p}_2}{(2\pi)^3} f_\chi(\vec{p}_1) f_\chi(\vec{p}_2)}, \quad (\text{A.16})$$

where function f is the WIMP phase-space distribution, usually taken as a Maxwell-Boltzmann distribution. The above expression can be further developed and simplified, and is finally found to be a temperature-dependent integral over simply two variables: s , the squared center-of-mass energy, and μ , the cosine of the angle between the annihilating particles — see [46, 47] for more details. As shown above, the integral over μ is performed analytically in our case. In practice, we compute $\langle \sigma v \rangle$ numerically from Eq. (A.16), where function $W(s)$ is tabulated up to $\sqrt{s - 4 m_\chi^2} = 10 m_\chi$, including all potential resonance and threshold effects. The Taylor expansion provided in Eq. (11) is only meant to clarify the discussion. It is indeed well known that such an expansion is a bad approximation in some cases [123]. Still, the S-wave expression given in Eq. (12) turns out to be quite accurate to compute the indirect detection signals, which is not surprising given that the WIMP velocity distribution in the Galaxy peaks around $x = m_\chi/T \approx 10^7$.

Appendix B. Relic density

We refer the reader to Refs. [46, 47] for more details on the relic density calculation, which we have followed in this study. We still provide a few pieces of information below, mostly related to the effective degrees of freedom, which is an independent part, except for the last paragraph which gives some information about the numerical algorithm.

Assuming entropy conservation and a Hubble rate set by the energy density ρ as $H^2 = 8\pi\rho/3$, the Boltzmann equation that drives the evolution of the dark matter fluid of density $n = s Y$ in the early universe reads:

$$\begin{aligned}\frac{dY}{dx} &= -\frac{1}{3H} \frac{ds}{dx} \frac{m_\chi}{x^2} \langle \sigma v \rangle (Y^2 - Y_{\text{eq}}^2) \\ &= -\sqrt{\frac{\pi}{45}} \frac{M_p m_\chi}{x^2} g_\star^{1/2} \langle \sigma v \rangle (Y^2 - Y_{\text{eq}}^2),\end{aligned}\quad (\text{B.1})$$

where M_p is the Planck mass, $s = (\rho + p)/3$ is the entropy density (p being the pressure). The dynamical variable is $x = m_\chi/T$, increasing when the universe expands. We further define the effective relativistic degrees of freedom g_{eff} and h_{eff} relevant to the energy density and the entropy density, respectively, such that:

$$\begin{aligned}\rho &= \frac{\pi^2}{30} g_{\text{eff}}(T) T^4 \\ s &= \frac{2\pi^2}{45} h_{\text{eff}}(T) T^3 \\ g_\star^{1/2} &= \frac{h_{\text{eff}}}{\sqrt{g_{\text{eff}}}} \left[1 + \frac{T}{3 h_{\text{eff}}} \frac{dh_{\text{eff}}}{dT} \right].\end{aligned}\quad (\text{B.2})$$

It is useful to recall the expressions of the energy density and the entropy density, for a fermion or a boson species labelled i :

$$\begin{aligned} \rho_{i,b/f}(T) &= g_i \int \frac{d^3 \vec{p}}{(2\pi)^3} \frac{E}{\exp\left\{\frac{E}{T}\right\} \mp 1} \\ s_{i,b/f} &= \frac{g_i}{T} \int \frac{d^3 \vec{p}}{(2\pi)^3} \frac{E + \vec{p} \cdot \vec{v}/3}{\exp\left\{\frac{E}{T}\right\} \mp 1} \end{aligned} \quad (\text{B.3})$$

These integrals can actually be evaluated quite easily from series involving modified Bessel functions of order n , K_n , which quickly converge to the exact results such that each species i carries [124]:

$$\begin{aligned} g_{\text{eff},i,b/f} &= \frac{15}{\pi^4} g_i \sum_{n=1}^{\infty} (\pm 1)^{n-1} \times \\ &\quad \left\{ \frac{x_i^3}{n} K_1(n x_i) + \frac{3 x_i^2}{n^2} K_2(n x_i) \right\} \\ h_{\text{eff},i,b/f} &= \frac{45}{4\pi^4} g_i \sum_{n=1}^{\infty} (\pm 1)^{n-1} \times \\ &\quad \left\{ \frac{x_i^3}{n} K_1(n x_i) + \frac{4 x_i^2}{n^2} K_2(n x_i) \right\}, \end{aligned} \quad (\text{B.4})$$

where $x_i = m_i/T$. Note that in the ultra-relativistic limit $x_i \rightarrow 0$, these expressions tend to g_i and $(7/8)g_i$, respectively for bosons and fermions, as expected. We have used the following property of Bessel functions [125]:

$$\int_y^{+\infty} (x^2 - y^2)^{\alpha-1} e^{-\mu x} dx = \frac{1}{\sqrt{\pi}} \left[\frac{2y}{\mu} \right]^{\frac{2\alpha-1}{2}} \Gamma(\alpha) K_{\frac{2\alpha-1}{2}}(\mu y).$$

Given these expressions, one can calculate the complete set of effective degrees of freedom by summing over all physical degrees of freedom at a given temperature. Before the QCD phase transition in the very early universe down to $T \sim M_W$, this amounts to all degrees of freedom of the standard model, including quarks and gluons, except the W^\pm , Z and Higgs bosons (the electroweak phase transition occurs earlier when $T \gtrsim M_W$). After the QCD phase transition, quarks and gluons are no longer free and remain confined into hadrons; then resonances have also to be included in addition to nucleons, an can provide extra-contribution depending on whether they are relativistic or not [126].

Note that in principle, one should also add those additional degrees of freedom coming from non-standard particles related to the particular dark matter model under scrutiny. In this paper, the light Higgs bosons and the singlino should therefore be added. Nevertheless, we can safely neglect them since they are also non-relativistic when singlino decouple, around $m_\chi/T \sim 20$ (we used $m_a \gtrsim 1$ GeV and $m_h \gtrsim 4$ GeV, and focused on $5 \text{ GeV} \lesssim m_\chi \lesssim 15 \text{ GeV}$). Our results are illustrated in Fig. 1, where a sharp QCD phase transition has been considered. Such a transition implies that g_\star goes to infinity because of the derivative of h_{eff} in Eq. (B.2). We have suppressed this divergence based on that the actual transition is expected to be smoother [54]. We have checked that considering this effect or not has no significant impact on our results, at the percent level.

As regards the numerical method, we have implemented a Runge-Kutta-6 scheme to track the evolution of the comoving density Y featuring Eq. (B.1). To avoid starting the calculation too early (too small x), we first estimate the decoupling temperature by implicitly solving Eq. (B.1), demanding $Y(x_\epsilon) = (1+\epsilon)Y_{\text{eq}}(x_\epsilon)$ (with $\epsilon < 1/2$, typically) — before decoupling, Y tracks its equilibrium value. We then start the calculation at $x_{\text{in}} \lesssim x_\epsilon$, up to after the decoupling. Indeed, to achieve an accuracy at the percent level, we need to solve Eq. (B.1) up to x_{end} such that $Y(x_{\text{end}}) > 10 Y_{\text{eq}}(x_{\text{end}})$, because of the term $(Y^2 - Y_{\text{eq}}^2)$. In practice, we use $Y(x_{\text{end}}) = 30 Y_{\text{eq}}(x_{\text{end}})$. Then, we neglect Y_{eq} and can therefore use the solution of Eq. (9), taking $x_{>f} = x_{\text{end}}$ and performing a Simpson integral over x in logarithmic steps.

References

- [1] C. E. Aalseth, P. S. Barbeau, N. S. Bowden, B. Cabrera-Palmer, J. Colaresi, J. I. Collar, S. Dazeley, P. de Lurgio, J. E. Fast, N. Fields, C. H. Greenberg, T. W. Hossbach, M. E. Keillor, J. D. Kephart, M. G. Marino, H. S. Miley, M. L. Miller, J. L. Orrell, D. C. Radford, D. Reyna, O. Tench, T. D. van Wechel, J. F. Wilkerson, K. M. Yocum, Results from a Search for Light-Mass Dark Matter with a p-Type Point Contact Germanium Detector, *Physical Review Letters* 106 (13) (2011) 131301–+. [arXiv:1002.4703](https://arxiv.org/abs/1002.4703), doi:10.1103/PhysRevLett.106.131301.
- [2] E. Aprile, K. Arisaka, F. Arneodo, A. Askin, L. Baudis, A. Behrens, K. Bokeloh, E. Brown, J. M. R. Cardoso, B. Choi, D. B. Cline, S. Fattori, A. D. Ferella, K. Giboni, A. Kish, C. W. Lam, J. Lamblin, R. F. Lang, K. E. Lim, J. A. M. Lopes, T. Marrodán Undagoitia, Y. Mei, A. J. Melgarejo Fernandez, K. Ni, U. Oberlack, S. E. A. Orrigo, E. Pantic, G. Plante, A. C. C. Ribeiro, R. Santorelli, J. M. F. Dos Santos, M. Schumann, P. Shagin, A. Teymourian, D. Thers, E. Tziaferi, H. Wang, C. Weinheimer, XENON100 Collaboration, First Dark Matter Results from the XENON100 Experiment, *Physical Review Letters* 105 (13) (2010) 131302–+. [arXiv:1005.0380](https://arxiv.org/abs/1005.0380), doi:10.1103/PhysRevLett.105.131302.
- [3] E. Aprile, K. Arisaka, F. Arneodo, A. Askin, L. Baudis, A. Behrens, K. Bokeloh, E. Brown, T. Bruch, G. Bruno, J. M. R. Cardoso, W. Chen, B. Choi, D. Cline, E. Duchovni, S. Fattori, A. D. Ferella, F. Gao, K. Giboni, E. Gross, A. Kish, C. W. Lam, J. Lamblin, R. F. Lang, C. Levy, K. E. Lim, Q. Lin, S. Lindemann, M. Lindner, J. A. M. Lopes, K. Lung, T. Marrodan Undagoitia, Y. Mei, A. J. Melgarejo Fernandez, K. Ni, U. Oberlack, S. E. A. Orrigo, E. Pantic, R. Persiani, G. Plante, A. C. C. Ribeiro, R. Santorelli, J. M. F. dos Santos, G. Sartorelli, M. Schumann, M. Selvi, P. Shagin, H. Simgen, A. Teymourian, D. Thers, O. Vitells, H. Wang, M. Weber, C. Weinheimer, Dark Matter Results from 100 Live Days of XENON100 Data, [arXiv:1104.2549](https://arxiv.org/abs/1104.2549).
- [4] M. Felizardo, T. Girard, T. Morlat, A. C. Fernandes, F. Giuliani, A. R. Ramos, J. G. Marques, M. Auguste, D. Boyer, A. Cavaillou, J. Poupény, C. Sudre, J. Puibasset, H. S. Miley, R. F. Payne, F. P. Carvalho, M. I. Prudêncio, R. Marques, Final Analysis and Results of the Phase II SIMPLE Dark Matter Search, [arXiv:1106.3014](https://arxiv.org/abs/1106.3014).
- [5] Z. Ahmed, D. S. Akerib, S. Arrenberg, C. N. Bailey, D. Balakishiyeva, L. Baudis, D. A. Bauer, P. L. Brink, T. Bruch, R. Bunker, B. Cabrera, D. O. Caldwell, J. Cooley, P. Cushman, M. Daal, F. DeJongh, M. R. Dragowsky, L. Duong, S. Fallows, E. Figueroa-Feliciano, J. Filippini, M. Fritts, S. R. Golwala, D. R. Grant, J. Hall, R. Hennings-Yeomans, S. A. Hertel, D. Holmgren, L. Hsu, M. E. Huber, O. Kamaev, M. Kiveni, M. Kos, S. W. Leman, R. Mahapatra, V. Mandic, K. A. McCarthy, N. Mirabolfathi, D. Moore, H. Nelson, R. W. Ogburn, A. Phipps, M. Pyle, X. Qiu, E. Ramberg, W. Rau, A. Reisetter, T. Saab, B. Sadoulet, J. Sander, R. W. Schnee, D. N. Seitz, B. Serfass, K. M. Sundqvist, M. Tarka, P. Wikus, S. Yellin, J. Yoo, B. A. Young, J. Zhang, Dark Matter Search Results from the CDMS II Experiment, *Science* 327 (2010) 1619–. [arXiv:0912.3592](https://arxiv.org/abs/0912.3592), doi:10.1126/science.1186112.
- [6] Z. Ahmed, D. S. Akerib, S. Arrenberg, C. N. Bailey, D. Balakishiyeva, L. Baudis, D. A. Bauer, P. L. Brink, T. Bruch, R. Bunker, B. Cabre-

- era, D. O. Caldwell, J. Cooley, E. Do Couto E Silva, P. Cushman, M. Daal, F. Dejongh, P. di Stefano, M. R. Dragowsky, L. Duong, S. Fallsows, E. Figueroa-Feliciano, J. Filippini, J. Fox, M. Fritts, S. R. Golwala, J. Hall, R. Hennings-Yeomans, S. A. Hertel, D. Holmgren, L. Hsu, M. E. Huber, O. Kamaev, M. Kiveni, M. Kos, S. W. Leman, S. Liu, R. Mahapatra, V. Mandic, K. A. McCarthy, N. Mirabolfathi, D. Moore, H. Nelson, R. W. Ogburn, A. Phipps, M. Pyle, X. Qiu, E. Ramberg, W. Rau, A. Reissetter, R. Resch, T. Saab, B. Sadoulet, J. Sander, R. W. Schnee, D. N. Seitz, B. Serfass, K. M. Sundqvist, M. Tarka, P. Wikus, S. Yellin, J. Yoo, B. A. Young, J. Zhang, Results from a Low-Energy Analysis of the CDMS II Germanium Data, *Physical Review Letters* 106 (13) (2011) 131302+. [arXiv:1011.2482](#), [doi:10.1103/PhysRevLett.106.131302](#).
- [7] C. E. Aalseth, P. S. Barbeau, J. Colaresi, J. I. Collar, J. Diaz Leon, J. E. Fast, N. Fields, T. W. Hossbach, M. E. Keillor, J. D. Kephart, A. Knecht, M. G. Marino, H. S. Miley, M. L. Miller, J. L. Orrell, D. C. Radford, J. F. Wilkerson, K. M. Yocum, Search for an Annual Modulation in a P-type Point Contact Germanium Dark Matter Detector, [arXiv:1106.0650](#).
- [8] A. Bottino, F. Donato, N. Fornengo, S. Scopel, Relic neutralinos and the two dark matter candidate events of the CDMS II experiment, *Phys. Rev. D* 81 (10) (2010) 107302+. [arXiv:0912.4025](#), [doi:10.1103/PhysRevD.81.107302](#).
- [9] J. Kopp, T. Schwetz, J. Zupan, Global interpretation of direct Dark Matter searches after CDMS-II results, *Journal of Cosmology and Astro-Particle Physics* 2 (2010) 14+. [arXiv:0912.4264](#), [doi:10.1088/1475-7516/2010/02/014](#).
- [10] Y. Mambrini, The kinetic dark-mixing in the light of CoGENT and XENON100, *JCAP* 9 (2010) 22+. [arXiv:1006.3318](#), [doi:10.1088/1475-7516/2010/09/022](#).
- [11] R. Bernabei, P. Belli, F. Cappella, R. Cerulli, F. Montecchia, F. Nozzoli, A. Incicchitti, D. Prosperi, C. J. Dai, H. H. Kuang, J. M. Ma, Z. P. Ye, Dark Matter search, *Nuovo Cimento Rivista Serie* 26 (1) (2003) 010000-74. [arXiv:astro-ph/0307403](#).
- [12] R. Bernabei, P. Belli, F. Cappella, R. Cerulli, C. J. Dai, A. D'Angelo, H. L. He, A. Incicchitti, H. H. Kuang, J. M. Ma, F. Montecchia, F. Nozzoli, D. Prosperi, X. D. Sheng, Z. P. Ye, First results from DAMA/LIBRA and the combined results with DAMA/NaI, *European Physical Journal C* (2008) 167+. [arXiv:0804.2741](#), [doi:10.1140/epjc/s10052-008-0662-y](#).
- [13] A. Bottino, F. Donato, N. Fornengo, S. Scopel, Compatibility of the new DAMA/NaI data on an annual modulation effect in WIMP direct search with a relic neutralino in supergravity schemes, *Phys. Rev. D* 59 (9) (1999) 095004+. [arXiv:hep-ph/9808459](#), [doi:10.1103/PhysRevD.59.095004](#).
- [14] M. T. Frandsen, F. Kahlhoefer, J. March-Russell, C. McCabe, M. McCullough, K. Schmidt-Hoberg, On the DAMA and CoGENT Modulations, [arXiv:1105.3734](#).
- [15] M. Farina, D. Pappadopulo, A. Strumia, T. Volansky, Can CoGENT and DAMA Modulations Be Due to Dark Matter?, [arXiv:1107.0715](#).
- [16] C. McCabe, DAMA and CoGENT without astrophysical uncertainties, [arXiv:1107.0741](#).
- [17] D. Albornoz Vásquez, G. Bélanger, C. Boehm, A. Pukhov, J. Silk, Can neutralinos in the MSSM and NMSSM scenarios still be light?, *Phys. Rev. D* 82 (11) (2010) 115027+. [arXiv:1009.4380](#), [doi:10.1103/PhysRevD.82.115027](#).
- [18] N. Fornengo, S. Scopel, A. Bottino, Discussing direct search of dark matter particles in the minimal supersymmetric extension of the standard model with light neutralinos, *Phys. Rev. D* 83 (1) (2011) 015001+. [arXiv:1011.4743](#), [doi:10.1103/PhysRevD.83.015001](#).
- [19] J. M. Cline, A. R. Frey, F. Chen, Metastable dark matter mechanisms for INTEGRAL 511 keV γ rays and DAMA/CoGENT events, *Phys. Rev. D* 83 (8) (2011) 083511+. [arXiv:1008.1784](#), [doi:10.1103/PhysRevD.83.083511](#).
- [20] A. V. Belikov, J. F. Guinon, D. Hooper, T. M. P. Tait, CoGENT, DAMA, and Light Neutralino Dark Matter, [arXiv:1009.0549](#).
- [21] J. F. Guinon, A. V. Belikov, D. Hooper, CoGENT, DAMA, and Neutralino Dark Matter in the Next-To-Minimal Supersymmetric Standard Model, [arXiv:1009.2555](#).
- [22] P. Draper, T. Liu, C. E. M. Wagner, L.-T. Wang, H. Zhang, Dark Light-Higgs Bosons, *Physical Review Letters* 106 (12) (2011) 121805+. [arXiv:1009.3963](#), [doi:10.1103/PhysRevLett.106.121805](#).
- [23] R. Kappl, M. Ratz, M. W. Winkler, Light dark matter in the singlet-extended MSSM, *Physics Letters B* 695 (2011) 169-173. [arXiv:1010.0553](#), [doi:10.1016/j.physletb.2010.10.063](#).
- [24] U. Ellwanger, M. Rausch de Trautenberg, C. A. Savoy, Phenomenology of supersymmetric models with a singlet, *Nuclear Physics B* 492 (1997) 21-50. [arXiv:hep-ph/9611251](#), [doi:10.1016/S0550-3213\(97\)80026-0](#).
- [25] U. Ellwanger, C. Hugonie, A. M. Teixeira, The Next-to-Minimal Supersymmetric Standard Model, *Phys. Rept.* 496 (2010) 1-77. [arXiv:0910.1785](#), [doi:10.1016/j.physrep.2010.07.001](#).
- [26] C. E. Aalseth, P. S. Barbeau, D. G. Cerdeño, J. Colaresi, J. I. Collar, P. de Lurgio, G. Drake, J. E. Fast, C. H. Greenberg, T. W. Hossbach, J. D. Kephart, M. G. Marino, H. S. Miley, J. L. Orrell, D. Reyna, R. G. H. Robertson, R. L. Talaga, O. Tench, T. D. van Wechel, J. F. Wilkerson, K. M. Yocum, Experimental Constraints on a Dark Matter Origin for the DAMA Annual Modulation Effect, *Physical Review Letters* 101 (25) (2008) 251301+. [arXiv:0807.0879](#), [doi:10.1103/PhysRevLett.101.251301](#).
- [27] J. Goodman, M. Ibe, A. Rajaraman, W. Shepherd, T. M. P. Tait, H. Yu, Constraints on light Majorana dark matter from colliders, *Physics Letters B* 695 (2011) 185-188. [arXiv:1005.1286](#), [doi:10.1016/j.physletb.2010.11.009](#).
- [28] J. Goodman, M. Ibe, A. Rajaraman, W. Shepherd, T. M. P. Tait, H. Yu, Constraints on dark matter from colliders, *Phys. Rev. D* 82 (11) (2010) 116010+. [arXiv:1008.1783](#), [doi:10.1103/PhysRevD.82.116010](#).
- [29] Y. Bai, P. J. Fox, R. Harnik, The Tevatron at the frontier of dark matter direct detection, *Journal of High Energy Physics* 12 (2010) 48+. [arXiv:1005.3797](#), [doi:10.1007/JHEP12\(2010\)048](#).
- [30] C. Arina, M. H. G. Tytgat, Constraints on light WIMP candidates from the isotropic diffuse gamma-ray emission, *JCAP* 1 (2011) 11+. [arXiv:1007.2765](#), [doi:10.1088/1475-7516/2011/01/011](#).
- [31] R. Kappl, M. W. Winkler, New limits on dark matter from Super-Kamiokande, *Nuclear Physics B* 850 (2011) 505-521. [arXiv:1104.0679](#), [doi:10.1016/j.nuclphysb.2011.05.006](#).
- [32] J. Laval, 10 GeV dark matter candidates and cosmic-ray antiprotons, *Phys. Rev. D* 82 (8) (2010) 081302+. [arXiv:1007.5253](#), [doi:10.1103/PhysRevD.82.081302](#).
- [33] G. Aad, B. Abbott, J. Abdallah, A. A. Abdelalim, A. Abdesselam, O. Abidinov, B. Abi, M. Abolins, H. Abramowicz, H. Abreu, et al., Search for Supersymmetry Using Final States with One Lepton, Jets, and Missing Transverse Momentum with the ATLAS Detector in $s=7\text{TeV}$ pp Collisions, *Physical Review Letters* 106 (13) (2011) 131802+. [arXiv:1102.2357](#), [doi:10.1103/PhysRevLett.106.131802](#).
- [34] Cms Collaboration, V. Khachatryan, A. M. Sirunyan, A. Tumasyan, W. Adam, T. Bergauer, M. Dragicevic, J. Erö, C. Fabjan, M. Friedl, et al., Search for supersymmetry in pp collisions at 7 TeV in events with jets and missing transverse energy, *Physics Letters B* 698 (2011) 196-218. [arXiv:1101.1628](#), [doi:10.1016/j.physletb.2011.03.021](#).
- [35] D. Treille, Searches at LEP, *Phys. Rept.* 403 (2004) 221-239. [doi:10.1016/j.physrep.2004.08.015](#).
- [36] F. Domingo, U. Ellwanger, E. Fullana, C. Hugonie, M.-A. Sanchez-Lozano, Radiative Upsilon decays and a light pseudoscalar Higgs in the NMSSM, *Journal of High Energy Physics* 1 (2009) 61+. [arXiv:0810.4736](#), [doi:10.1088/1126-6708/2009/01/061](#).
- [37] M. Iwasaki, K. Itoh, H. Aihara, K. Abe, K. Abe, I. Adachi, Y. Asano, T. Aushev, S. Bahinipati, A. M. Bakich, S. Banerjee, I. Bedny, U. Bitenc, I. Bizjak, S. Blyth, A. Bondar, A. Bozek, M. Bračko, J. Brodzicka, T. E. Browder, M.-C. Chang, P. Chang, Y. Chao, A. Chen, K.-F. Chen, W. T. Chen, B. G. Cheon, R. Chistov, S.-K. Choi, Y. Choi, A. Chuvikov, J. Dalseno, M. Danilov, M. Dash, A. Drutskoy, S. Eidelman, Y. Enari, S. Fratina, N. Gabyshev, T. Gershon, G. Gokhroo, B. Golob, A. Gorišek, J. Haba, T. Hara, N. C. Hastings, K. Hayasaka, H. Hayashii, M. Hazumi, T. Hokuue, Y. Hoshi, S. Hou, W.-S. Hou, Y. B. Hsiung, T. Iijima, A. Imoto, K. Inami, A. Ishikawa, H. Ishino, R. Itoh, J. H. Kang, J. S. Kang, N. Katayama, H. Kawai, T. Kawasaki, H. R. Khan, H. Kichimi, H. J. Kim, S. K. Kim, S. M. Kim, K. Kinoshita, P. Križan, P. Krokovny, R. Kulasiri, S. Kumar, C. C. Kuo, A. Kuzmin, Y.-J. Kwon, J. S. Lange, G. Leder, S. E. Lee, T. Lesiak, J. Li, S.-W. Lin, D. Liventsev, J. MacNaughton, G. Majumder, F. Mandl, T. Matsumoto, A. Matyja, Y. Mikami, W. Mitaroff, K. Miyabayashi, H. Miyake,

- H. Miyata, R. Mizuk, D. Mohapatra, G. R. Moloney, T. Nagamine, Y. Nagasaka, I. Nakamura, E. Nakano, M. Nakao, H. Nakazawa, Z. Natkaniec, S. Nishida, O. Nitoh, S. Ogawa, T. Ohshima, T. Okabe, S. Okuno, S. L. Olsen, W. Ostrowicz, H. Ozaki, H. Palka, C. W. Park, H. Park, N. Parslow, L. S. Peak, R. Pestotnik, L. E. Piilonen, N. Root, M. Rozanska, H. Sagawa, Y. Sakai, N. Sato, T. Schietinger, O. Schneider, P. Schönmeier, J. Schümann, C. Schwanda, A. J. Schwartz, M. E. Sevier, H. Shibuya, B. Shwartz, V. Sidorov, J. B. Singh, A. Somov, N. Soni, R. Stamen, S. Stanič, M. Starič, K. Sumisawa, T. Sumiyoshi, S. Suzuki, S. Y. Suzuki, O. Tajima, F. Takasaki, K. Tamai, N. Tamura, M. Tanaka, G. N. Taylor, Y. Teramoto, X. C. Tian, T. Tsukamoto, S. Uehara, T. Uglov, K. Ueno, S. Uno, P. Urquijo, Y. Ushiroda, G. Varner, K. E. Varvell, S. Villa, C. C. Wang, C. H. Wang, M.-Z. Wang, Y. Watanabe, Q. L. Xie, B. D. Yabsley, A. Yamaguchi, Y. Yamashita, M. Yamauchi, H. Yang, J. Ying, L. M. Zhang, Z. P. Zhang, V. Zhilich, D. Žontar, D. Zürcher, Improved measurement of the electroweak penguin process $B \rightarrow X_s l^+ l^-$, Phys. Rev. D72 (9) (2005) 092005+. arXiv:hep-ex/0503044, doi:10.1103/PhysRevD.72.092005.
- [38] A. Ali, E. Lunghi, C. Greub, G. Hiller, Improved model-independent analysis of semileptonic and radiative rare B decays, Phys. Rev. D66 (3) (2002) 034002+. arXiv:hep-ph/0112300, doi:10.1103/PhysRevD.66.034002.
- [39] M. Acciarri, O. Adriani, M. Aquilar-Benitez, S. Ahlen, B. Alpat, J. Alcaraz, G. Alemanni, J. Allaby, A. Aloisio, G. Alverson, et al., Search for neutral Higgs boson production through the process $e^+e^- \rightarrow Z^*H^0$, Physics Letters B 385 (1996) 454–470. doi:10.1016/0370-2693(96)00987-2.
- [40] W. Love, V. Savinov, H. Mendez, J. Y. Ge, D. H. Miller, I. P. J. Shipsey, B. Xin, G. S. Adams, M. Anderson, J. P. Cummings, I. Danko, D. Hu, B. Moziak, J. Napolitano, Q. He, J. Insler, H. Muramatsu, C. S. Park, E. H. Thorndike, F. Yang, M. Artuso, S. Blusk, S. Khalil, J. Li, R. Mountaint, S. Nisar, K. Randrianarivony, N. Sultana, T. Skwarnicki, S. Stone, J. C. Wang, L. M. Zhang, G. Bonvicini, D. Cinabro, M. Dubrovin, A. Lincoln, P. Naik, J. Rademacker, D. M. Asner, K. W. Edwards, J. Reed, R. A. Briere, T. Ferguson, G. Tatishvili, H. Vogel, M. E. Watkins, J. L. Rosner, J. P. Alexander, D. G. Cassel, J. E. Duboscq, R. Ehrlich, L. Fields, R. S. Galik, L. Gibbons, R. Gray, S. W. Gray, D. L. Hartill, B. K. Heltsley, D. Hertz, J. M. Hunt, J. Kandaswamy, D. L. Kreinick, V. E. Kuznetsov, J. Ledoux, H. Mahlke-Krüger, D. Mohapatra, P. U. E. Onyisi, J. R. Patterson, D. Peterson, D. Riley, A. Ryd, A. J. Sadoff, X. Shi, S. Stroiney, W. M. Sun, T. Wilksen, S. B. Athar, R. Patel, J. Yelton, P. Rubin, B. I. Eisenstein, I. Karliner, S. Mehrabyan, N. Lowrey, M. Selen, E. J. White, J. Wiss, R. E. Mitchell, M. R. Shepherd, D. Besson, T. K. Pedlar, D. Cronin-Hennessy, K. Y. Gao, J. Hietala, Y. Kubota, T. Klein, B. W. Lang, R. Poling, A. W. Scott, P. Zweber, S. Dobbs, Z. Metreveli, K. K. Seth, A. Tomaradze, J. Libby, L. Martin, A. Powell, G. Wilkinson, K. M. Ecklund, Search for Very Light CP-Odd Higgs Boson in Radiative Decays of Upsilon(1S), Physical Review Letters 101 (15) (2008) 151802+. arXiv:0807.1427, doi:10.1103/PhysRevLett.101.151802.
- [41] P. Salati, Quintessence and the relic density of neutralinos, Physics Letters B 571 (2003) 121–131. arXiv:astro-ph/0207396, doi:10.1016/j.physletb.2003.07.073.
- [42] E. W. Kolb, S. Wolfram, Baryon number generation in the early universe, Nuclear Physics B 172 (1980) 224–284. doi:10.1016/0550-3213(80)90167-4.
- [43] P. Binétruy, G. Girardi, P. Salati, Constraints on a system of two neutral fermions from cosmology, Nuclear Physics B 237 (1984) 285–306. doi:10.1016/0550-3213(84)90161-5.
- [44] M. Srednicki, R. Watkins, K. A. Olive, Calculations of relic densities in the early universe, Nuclear Physics B 310 (1988) 693–713. doi:10.1016/0550-3213(88)90099-5.
- [45] E. W. Kolb, M. S. Turner, The early universe, Frontiers in Physics, Reading, MA: Addison-Wesley, 1988, 1990, 1990.
- [46] P. Gondolo, G. Gelmini, Cosmic abundances of stable particles: improved analysis., Nuclear Physics B 360 (1991) 145–179. doi:10.1016/0550-3213(91)90438-4.
- [47] J. Edsjö, P. Gondolo, Neutralino relic density including coannihilations, Phys. Rev. D56 (1997) 1879–1894. arXiv:hep-ph/9704361, doi:10.1103/PhysRevD.56.1879.
- [48] P. Gondolo, J. Edsjö, P. Ullio, L. Bergström, M. Schelke, E. A. Baltz, DarkSUSY: computing supersymmetric dark matter properties numerically, JCAP7 (2004) 8+. arXiv:astro-ph/0406204, doi:10.1088/1475-7516/2004/07/008.
- [49] G. Bélanger, F. Boudjema, A. Pukhov, A. Semenov, micrOMEGAS: A program for calculating the relic density in the MSSM, Computer Physics Communications 149 (2002) 103–120. arXiv:hep-ph/0112278, doi:10.1016/S0010-4655(02)00596-9.
- [50] M. Drees, M. Kakizaki, S. Kulkarni, Thermal abundance of semirelativistic relics, Phys. Rev. D80 (4) (2009) 043505+. arXiv:0904.3046, doi:10.1103/PhysRevD.80.043505.
- [51] D. J. Fixsen, The Temperature of the Cosmic Microwave Background, Astrophys. J.707 (2009) 916–920. arXiv:0911.1955, doi:10.1088/0004-637X/707/2/916.
- [52] C. E. Detar, U. M. Heller, QCD thermodynamics from the lattice, European Physical Journal A 41 (2009) 405–437. arXiv:0905.2949, doi:10.1140/epja/i2009-10825-3.
- [53] A. Hietanen, K. Kajantie, M. Laine, K. Rummukainen, Y. Schröder, Three-dimensional physics and the pressure of hot QCD, Phys. Rev. D79 (4) (2009) 045018+. arXiv:0811.4664, doi:10.1103/PhysRevD.79.045018.
- [54] M. Hindmarsh, O. Philipsen, Dark matter of weakly interacting massive particles and the QCD equation of state, Phys. Rev. D71 (8) (2005) 087302+. arXiv:hep-ph/0501232, doi:10.1103/PhysRevD.71.087302.
- [55] D. Larson, J. Dunkley, G. Hinshaw, E. Komatsu, M. R.olta, C. L. Bennett, B. Gold, M. Halpern, R. S. Hill, N. Jarosik, A. Kogut, M. Limon, S. S. Meyer, N. Odegard, L. Page, K. M. Smith, D. N. Spergel, G. S. Tucker, J. L. Weiland, E. Wollack, E. L. Wright, Seven-year Wilkinson Microwave Anisotropy Probe (WMAP) Observations: Power Spectra and WMAP-derived Parameters, Astrophys. J. Suppl. Series192 (2011) 16+. arXiv:1001.4635, doi:10.1088/0067-0049/192/2/16.
- [56] A. Bottino, F. Donato, N. Fornengo, S. Scopel, Lower bound on the neutralino mass from new data on CMB and implications for relic neutralinos, Phys. Rev. D68 (4) (2003) 043506+. arXiv:hep-ph/0304080, doi:10.1103/PhysRevD.68.043506.
- [57] G. Jungman, M. Kamionkowski, K. Griest, Supersymmetric dark matter, Phys. Rept.267 (1996) 195–373. arXiv:hep-ph/9506380, doi:10.1016/0370-1573(95)00058-5.
- [58] M. M. Pavan, I. I. Strakovsky, R. L. Workman, R. A. Arndt, The pion-nucleon Sigma term is definitely large: results from a G.W.U. analysis of pion nucleon scattering data, PiN Newslett. 16 (2002) 110–115. arXiv:hep-ph/0111066.
- [59] T. Schwetz, Direct detection data and possible hints for low-mass WIMPs, arXiv:1011.5432.
- [60] A. Bottino, F. Donato, N. Fornengo, S. Scopel, Implications for relic neutralinos of the theoretical uncertainties in the neutralino-nucleon cross section, Astroparticle Physics 13 (2000) 215–225. arXiv:hep-ph/9909228, doi:10.1016/S0927-6505(99)00122-X.
- [61] A. Bottino, F. Donato, N. Fornengo, S. Scopel, Size of the neutralino-nucleon cross-section in the light of a new determination of the pion-nucleon sigma term, Astroparticle Physics 18 (2002) 205–211. arXiv:hep-ph/0111229, doi:10.1016/S0927-6505(02)00107-X.
- [62] J. Ellis, K. A. Olive, Y. Santoso, V. C. Spanos, Update on the direct detection of supersymmetric dark matter, Phys. Rev. D71 (9) (2005) 095007+. arXiv:hep-ph/0502001, doi:10.1103/PhysRevD.71.095007.
- [63] J. Ellis, K. A. Olive, C. Savage, Hadronic uncertainties in the elastic scattering of supersymmetric dark matter, Phys. Rev. D77 (6) (2008) 065026+. arXiv:0801.3656, doi:10.1103/PhysRevD.77.065026.
- [64] P. Belli, R. Bernabei, A. Bottino, F. Cappella, R. Cerulli, N. Fornengo, S. Scopel, Observations of annual modulation in direct detection of relic particles and light neutralinos, arXiv:1106.4667.
- [65] J. Silk, M. Srednicki, Cosmic-ray antiprotons as a probe of a photino-dominated universe, Physical Review Letters 53 (1984) 624–627.
- [66] S. Rudaz, F. W. Stecker, Cosmic-ray antiprotons, positrons, and gamma rays from halo dark matter annihilation, Astrophys. J.325 (1988) 16–25. doi:10.1086/165980.
- [67] A. Bottino, F. Donato, N. Fornengo, P. Salati, Which fraction of the measured cosmic-ray antiprotons might be due to neutralino annihilation in the galactic halo?, Phys. Rev. D58 (12) (1998) 123503+. arXiv:

- astro-ph/9804137.
- [68] L. Bergström, J. Edsjö, P. Ullio, Cosmic Antiprotons as a Probe for Supersymmetric Dark Matter?, *Astrophys. J.*526 (1999) 215–235. [arXiv:astro-ph/9902012](#), doi:10.1086/307975.
- [69] F. Donato, N. Fornengo, D. Maurin, P. Salati, R. Taillet, Antiprotons in cosmic rays from neutralino annihilation, *Phys. Rev. D*69 (6) (2004) 063501+. [arXiv:astro-ph/0306207](#), doi:10.1103/PhysRevD.69.063501.
- [70] A. M. Lionetto, A. Morselli, V. Zdravkovic, Uncertainties of cosmic ray spectra and detectability of antiproton mSUGRA contributions with PAMELA, *Journal of Cosmology and Astro-Particle Physics* 9 (2005) 0. doi:10.1088/1475-7516/2005/09/010.
- [71] J. Lavalle, E. Nezri, E. Athanassoula, F.-S. Ling, R. Teyssier, Antimatter cosmic rays from dark matter annihilation: First results from an N-body experiment, *Phys. Rev. D*78 (10) (2008) 103526+. [arXiv:0808.0332](#), doi:10.1103/PhysRevD.78.103526.
- [72] A. Barrau, P. Salati, G. Servant, F. Donato, J. Grain, D. Maurin, R. Taillet, Kaluza-Klein dark matter and galactic antiprotons, *Phys. Rev. D*72 (6) (2005) 063507. doi:10.1103/PhysRevD.72.063507.
- [73] O. Adriani, G. C. Barbarino, G. A. Bazilevskaia, R. Bellotti, M. Boezio, E. A. Bogomolov, L. Bonechi, M. Bongi, V. Bonvicini, S. Borisov, S. Bottai, A. Bruno, F. Cafagna, D. Campana, R. Carbone, P. Carlson, M. Casolino, G. Castellini, L. Consiglio, M. P. de Pascale, C. de Santis, N. de Simone, V. di Felice, A. M. Galper, W. Gillard, L. Grishantseva, P. Hofverberg, G. Jerse, A. V. Karelin, S. V. Koldashov, S. Y. Krutkov, A. N. Kvashnin, A. Leonov, V. Malvezzi, L. Marcelli, A. G. Mayorov, W. Menn, V. V. Mikhailov, E. Mocchiutti, A. Monaco, N. Mori, N. Nikonov, G. Osteria, P. Papini, M. Pearce, P. Picozza, C. Pizzolotto, M. Ricci, S. B. Ricciarini, L. Rossetto, M. Simon, R. Sparvoli, P. Spillantini, Y. I. Stozhkov, A. Vacchi, E. Vannuccini, G. Vasilyev, S. A. Voronov, J. Wu, Y. T. Yurkin, G. Zampa, N. Zampa, V. G. Zverev, PAMELA Collaboration, PAMELA Results on the Cosmic-Ray Antiproton Flux from 60 MeV to 180 GeV in Kinetic Energy, *Physical Review Letters* 105 (12) (2010) 121101+. [arXiv:1007.0821](#), doi:10.1103/PhysRevLett.105.121101.
- [74] S. Orito, T. Maeno, H. Matsunaga, K. Abe, K. Anraku, Y. Asaoka, M. Fujikawa, M. Imori, M. Ishino, Y. Makida, N. Matsui, H. Matsumoto, J. Mitchell, T. Mitsui, A. Moiseev, M. Motoki, J. Nishimura, M. Nozaki, J. Ormes, T. Saeki, T. Sanuki, M. Sasaki, E. S. Seo, Y. Shikaze, T. Sonoda, R. Streitmatter, J. Suzuki, K. Tanaka, I. Ueda, N. Yajima, T. Yamagami, A. Yamamoto, T. Yoshida, K. Yoshimura, Precision Measurement of Cosmic-Ray Antiproton Spectrum, *Physical Review Letters* 84 (2000) 1078–1081. [arXiv:astro-ph/9906426](#).
- [75] T. Maeno, S. Orito, H. Matsunaga, K. Abe, K. Anraku, Y. Asaoka, M. Fujikawa, M. Imori, Y. Makida, N. Matsui, H. Matsumoto, J. Mitchell, T. Mitsui, A. Moiseev, M. Motoki, J. Nishimura, M. Nozaki, J. Ormes, T. Saeki, T. Sanuki, M. Sasaki, E. S. Seo, Y. Shikaze, T. Sonoda, R. Streitmatter, J. Suzuki, K. Tanaka, I. Ueda, J. Z. Wang, N. Yajima, T. Yamagami, A. Yamamoto, T. Yoshida, K. Yoshimura, Successive measurements of cosmic-ray antiproton spectrum in a positive phase of the solar cycle, *Astroparticle Physics* 16 (2001) 121–128. [arXiv:astro-ph/0010381](#).
- [76] Y. Asaoka, Y. Shikaze, K. Abe, K. Anraku, M. Fujikawa, H. Fuke, S. Haino, M. Imori, K. Izumi, T. Maeno, Y. Makida, S. Matsuda, N. Matsui, T. Matsukawa, H. Matsumoto, H. Matsunaga, J. Mitchell, T. Mitsui, A. Moiseev, M. Motoki, J. Nishimura, M. Nozaki, S. Orito, J. F. Ormes, T. Saeki, T. Sanuki, M. Sasaki, E. S. Seo, T. Sonoda, R. Streitmatter, J. Suzuki, K. Tanaka, K. Tanizaki, I. Ueda, J. Z. Wang, Y. Yajima, Y. Yamagami, A. Yamamoto, Y. Yamamoto, K. Yamato, T. Yoshida, K. Yoshimura, Measurements of Cosmic-Ray Low-Energy Antiproton and Proton Spectra in a Transient Period of Solar Field Reversal, *Physical Review Letters* 88 (5) (2002) 051101+. [arXiv:astro-ph/0109007](#).
- [77] S. Haino, et al., Measurement of cosmic-ray antiproton spectrum with BESS-2002, in: *International Cosmic Ray Conference*, Vol. 3 of International Cosmic Ray Conference, 2005, pp. 13–+.
- [78] F. Donato, D. Maurin, P. Salati, A. Barrau, G. Boudoul, R. Taillet, Antiprotons from Spallations of Cosmic Rays on Interstellar Matter, *Astrophys. J.*563 (2001) 172–184.
- [79] T. Bringmann, P. Salati, Galactic antiproton spectrum at high energies: Background expectation versus exotic contributions, *Phys. Rev. D*75 (8) (2007) 083006. doi:10.1103/PhysRevD.75.083006.
- [80] I. V. Moskalenko, A. W. Strong, J. F. Ormes, M. S. Potgieter, Secondary Antiprotons and Propagation of Cosmic Rays in the Galaxy and Heliosphere, *Astrophys. J.*565 (2002) 280–296. doi:10.1086/324402.
- [81] R. Trotta, G. Jóhannesson, I. V. Moskalenko, T. A. Porter, R. Ruiz de Austri, A. W. Strong, Constraints on Cosmic-ray Propagation Models from A Global Bayesian Analysis, *Astrophys. J.*729 (2011) 106–+. [arXiv:1011.0037](#), doi:10.1088/0004-637X/729/2/106.
- [82] A. Bottino, F. Donato, N. Fornengo, P. Salati, Antiproton fluxes from light neutralinos, *Phys. Rev. D*72 (8) (2005) 083518+. [arXiv:hep-ph/0507086](#), doi:10.1103/PhysRevD.72.083518.
- [83] A. Putze, L. Derome, D. Maurin, A Markov Chain Monte Carlo technique to sample transport and source parameters of Galactic cosmic rays. II. Results for the diffusion model combining B/C and radioactive nuclei, *Astron. Astroph.*516 (2010) A66+. [arXiv:1001.0551](#), doi:10.1051/0004-6361/201014010.
- [84] R. Catena, P. Ullio, A novel determination of the local dark matter density, *JCAP*8 (2010) 4+. [arXiv:0907.0018](#), doi:10.1088/1475-7516/2010/08/004.
- [85] P. Salucci, F. Nesti, G. Gentile, C. Frigerio Martins, The dark matter density at the Sun’s location, *Astron. Astroph.*523 (2010) A83+. [arXiv:1003.3101](#), doi:10.1051/0004-6361/201014385.
- [86] T. Sjöstrand, S. Mrenna, P. Skands, PYTHIA 6.4 physics and manual, *Journal of High Energy Physics* 5 (2006) 26–+. [arXiv:hep-ph/0603175](#), doi:10.1088/1126-6708/2006/05/026.
- [87] K. Nakamura, Particle Data Group, Review of Particle Physics, *Journal of Physics G Nuclear Physics* 37 (7) (2010) 075021+. doi:10.1088/0954-3899/37/7A/075021.
- [88] J. F. Navarro, C. S. Frenk, S. D. M. White, A Universal Density Profile from Hierarchical Clustering, *Astrophys. J.*490 (1997) 493–+. [arXiv:astro-ph/9611107](#), doi:10.1086/304888.
- [89] H. Zhao, Analytical models for galactic nuclei, *MNRAS*278 (1996) 488–496. [arXiv:astro-ph/9509122](#).
- [90] J. Einasto, On constructing models of stellar systems. II. The descriptive functions and parameters., *Publications of the Tartu Astrofizica Observatory* 36 (1968) 357–378.
- [91] D. Merritt, A. W. Graham, B. Moore, J. Diemand, B. Terzić, Empirical Models for Dark Matter Halos. I. Nonparametric Construction of Density Profiles and Comparison with Parametric Models, *Astron. J.*132 (2006) 2685–2700. [arXiv:astro-ph/0509417](#), doi:10.1086/508988.
- [92] J. F. Navarro, A. Ludlow, V. Springel, J. Wang, M. Vogelsberger, S. D. M. White, A. Jenkins, C. S. Frenk, A. Helmi, The diversity and similarity of simulated cold dark matter haloes, *MNRAS*402 (2010) 21–34. [arXiv:0810.1522](#), doi:10.1111/j.1365-2966.2009.15878.x.
- [93] F. Governato, C. Brook, L. Mayer, A. Brooks, G. Rhee, J. Wadsley, P. Jonsson, B. Willman, G. Stinson, T. Quinn, P. Madau, Bulgeless dwarf galaxies and dark matter cores from supernova-driven outflows, *Nature*463 (2010) 203–206. doi:10.1038/nature08640.
- [94] W. J. G. de Blok, The Core-Cusp Problem, *Advances in Astronomy* 2010. [arXiv:0910.3538](#), doi:10.1155/2010/789293.
- [95] P. J. McMillan, Mass models of the Milky Way, *MNRAS*(2011) 553–+[arXiv:1102.4340](#), doi:10.1111/j.1365-2966.2011.18564.x.
- [96] J. Silk, A. Stebbins, Clumpy cold dark matter, *Astrophys. J.*411 (1993) 439–449. doi:10.1086/172846.
- [97] T. Bringmann, Particle models and the small-scale structure of dark matter, *New Journal of Physics* 11 (10) (2009) 105027+. [arXiv:0903.0189](#), doi:10.1088/1367-2630/11/10/105027.
- [98] J. Lavalle, Q. Yuan, D. Maurin, X.-J. Bi, Full calculation of clumpiness boost factors for antimatter cosmic rays in the light of Λ CDM N-body simulation results. Abandoning hope in clumpiness enhancement?, *Astron. Astroph.*479 (2008) 427–452. [arXiv:0709.3634](#), doi:10.1051/0004-6361:20078723.
- [99] L. Pieri, J. Lavalle, G. Bertone, E. Branchini, Implications of high-resolution simulations on indirect dark matter searches, *Phys. Rev. D*83 (2) (2011) 023518–+. [arXiv:0908.0195](#), doi:10.1103/PhysRevD.83.023518.
- [100] A. W. Strong, I. V. Moskalenko, Propagation of Cosmic-Ray Nucleons in the Galaxy, *Astrophys. J.*509 (1998) 212–228. [arXiv:astro-ph/9807150](#), doi:10.1086/306470.

- [101] V. S. Berezhinskii, S. V. Bulanov, V. A. Dogiel, V. S. Ptuskin, *Astrophysics of cosmic rays*, Amsterdam: North-Holland, edited by Ginzburg, V.L., 1990.
- [102] V. S. Ptuskin, H. J. Voelk, V. N. Zirakashvili, D. Breitschwerdt, Transport of relativistic nucleons in a galactic wind driven by cosmic rays., *Astron. Astroph.*321 (1997) 434–443.
- [103] D. Maurin, F. Donato, R. Taïllet, P. Salati, Cosmic Rays below $Z=30$ in a Diffusion Model: New Constraints on Propagation Parameters, *Astrophys. J.*555 (2001) 585–596. [arXiv:astro-ph/0101231](#), doi: 10.1086/321496.
- [104] L. J. Gleeson, W. I. Axford, Solar Modulation of Galactic Cosmic Rays, *Astrophys. J.*154 (1968) 1011–+. doi:10.1086/149822.
- [105] L. A. Fisk, Solar modulation of galactic cosmic rays, 2., *J. Geophys. Res.*76 (1971) 221–226. doi:10.1029/JA076i001p00221.
- [106] A. W. Strong, I. V. Moskalenko, V. S. Ptuskin, Cosmic-Ray Propagation and Interactions in the Galaxy, *Annual Review of Nuclear and Particle Science* 57 (2007) 285–327. [arXiv:astro-ph/0701517](#), doi:10.1146/annurev.nucl.57.090506.123011.
- [107] J. S. Perko, Solar modulation of galactic antiprotons, *Astron. Astroph.*184 (1987) 119–121.
- [108] Y. Shikaze, S. Haino, K. Abe, H. Fuke, T. Hams, K. C. Kim, Y. Makida, S. Matsuda, J. W. Mitchell, A. A. Moiseev, J. Nishimura, M. Nozaki, S. Orito, J. F. Ormes, T. Sanuki, M. Sasaki, E. S. Seo, R. E. Streitmatter, J. Suzuki, K. Tanaka, T. Yamagami, A. Yamamoto, T. Yoshida, K. Yoshimura, Measurements of 0.2–20 GeV/n cosmic-ray proton and helium spectra from 1997 through 2002 with the BESS spectrometer, *Astroparticle Physics* 28 (2007) 154–167. [arXiv:astro-ph/0611388](#), doi:10.1016/j.astropartphys.2007.05.001.
- [109] M. S. Potgieter, The dynamic heliosphere, solar activity, and cosmic rays, *Advances in Space Research* 46 (2010) 402–412. doi:10.1016/j.asr.2009.09.016.
- [110] E. N. Parker, The passage of energetic charged particles through interplanetary space, *Planetary and Space Science*13 (1965) 9–+. doi: 10.1016/0032-0633(65)90131-5.
- [111] R. A. Mewaldt, A. J. Davis, K. A. Lave, R. A. Leske, E. C. Stone, M. E. Wiedenbeck, W. R. Binns, E. R. Christian, A. C. Cummings, G. A. de Nolfo, M. H. Israel, A. W. Labrador, T. T. von Rosenvinge, Record-setting Cosmic-ray Intensities in 2009 and 2010, *Astrophys. J. Lett.*723 (2010) L1–L6. doi:10.1088/2041-8205/723/1/L1.
- [112] F. C. Jones, A. Lukasiak, V. Ptuskin, W. Webber, The Modified Weighted Slab Technique: Models and Results, *Astrophys. J.*547 (2001) 264–271. [arXiv:astro-ph/0007293](#), doi:10.1086/318358.
- [113] T. Delahaye, R. Lineros, F. Donato, N. Fornengo, P. Salati, Positrons from dark matter annihilation in the galactic halo: Theoretical uncertainties, *Phys. Rev. D*77 (6) (2008) 063527–+. [arXiv:0712.2312](#), doi:10.1103/PhysRevD.77.063527.
- [114] T. Delahaye, F. Donato, N. Fornengo, J. Lavalle, R. Lineros, P. Salati, R. Taïllet, Galactic secondary positron flux at the Earth, *Astron. Astroph.*501 (2009) 821–833. [arXiv:0809.5268](#), doi:10.1051/0004-6361/200811130.
- [115] J. Lavalle, Impact of the spectral hardening of TeV cosmic rays on the prediction of the secondary positron flux, *MNRAS*414 (2011) 985–991. [arXiv:1011.3063](#), doi:10.1111/j.1365-2966.2011.18294.x.
- [116] T. Bringmann, F. Donato, R. A. Lineros, Radio data and synchrotron emission in consistent cosmic ray models, [arXiv:1106.4821](#).
- [117] J. M. Cline, A. R. Frey, Minimal hidden sector models for CoGeNT/DAMA events, [arXiv:1108.1391](#).
- [118] D. G. Cerdeno, J.-H. Huh, M. Peiro, O. Seto, Very light right-handed sneutrino dark matter in the NMSSM, [arXiv:1108.0978](#).
- [119] J. Cao, K.-i. Hikasa, W. Wang, J. M. Yang, Light dark matter in NMSSM and implication on Higgs phenomenology, [arXiv:1104.1754](#).
- [120] D. Albornoz Vasquez, G. Belanger, C. Boehm, Astrophysical limits on light NMSSM neutralinos, [arXiv:1107.1614](#).
- [121] D. T. Cumberbatch, D. E. López-Fogliani, L. Roszkowski, R. Ruiz de Austri, Y.-L. S. Tsai, Is light neutralino as dark matter still viable?, [arXiv:1107.1604](#).
- [122] V. Berezhinsky, V. Dokuchaev, Y. Eroshenko, Destruction of small-scale dark matter clumps in the hierarchical structures and galaxies, *Phys. Rev. D*73 (6) (2006) 063504–+. [arXiv:astro-ph/0511494](#), doi: 10.1103/PhysRevD.73.063504.
- [123] K. Griest, D. Seckel, Three exceptions in the calculation of relic abundances, *Phys. Rev. D*43 (1991) 3191–3203. doi:10.1103/PhysRevD.43.3191.
- [124] A. Bouquet, P. Salati, J. Silk, gamma -ray lines as a probe for a cold-dark-matter halo, *Phys. Rev. D*40 (1989) 3168–3186. doi:10.1103/PhysRevD.40.3168.
- [125] M. Abramowitz, I. A. Stegun, *Handbook of Mathematical Functions*, New York: Dover, 1972.
- [126] S. Sarkar, Big bang nucleosynthesis and physics beyond the standard model, *Reports on Progress in Physics* 59 (1996) 1493–1609. [arXiv:hep-ph/9602260](#), doi:10.1088/0034-4885/59/12/001.